

1 Protein tyrosine phosphatase receptor kappa regulates glycolysis and *de novo* lipogenesis 2 to promote hepatocyte metabolic reprogramming in obesity

3 Eduardo H. Gilgioni¹, Ao Li¹, Wadsen St-Pierre-Wijckmans¹, Tzu-Keng Shen^{1,2,3,4}, Israel
4 Pérez-Chávez^{1,2,3,4}, Garnik Hovhannisyan¹, Michela Lisjak¹, Javier Negueruela¹, Valerie
5 Vandembemt¹, Julia Bauzá-Martinez⁵, Jose M. Herranz⁶, Daria Ezerina^{2,3,4}, Stephane
6 Demine¹, Zheng Feng¹, Thibaut Vignane⁷, Lukas Otero-Sánchez^{8,9}, Flavia Lambertucci¹,
7 Alena Prašnická¹, Jacques Devière^{8,9}, David C. Hay¹⁰, Jose A. Encinar¹¹, Sumeet Pal Singh¹²,
8 Joris Messens^{2,3,4}, Milos R. Filipovic⁸, Hayley J. Sharpe¹³, Eric Trépo^{9,10}, Wei Wu^{5,14,15} and
9 Esteban N. Gurzov^{1,16}

10

11 ¹Signal Transduction and Metabolism Laboratory, Université libre de Bruxelles, Brussels B-
12 1070, Belgium.

13 ²VIB-VUB Center for Structural Biology, Vlaams Instituut voor Biotechnologie, Brussels B-
14 1050, Belgium.

15 ³Structural Biology Brussels, Vrije Universiteit Brussel, Brussels B-1050, Belgium.

16 ⁴Brussels Center for Redox Biology, Vrije Universiteit Brussel, Brussels B-1050, Belgium.

17 ⁵Biomolecular Mass Spectrometry and Proteomics, Bijvoet Center for Biomolecular Research
18 and Utrecht Institute for Pharmaceutical Sciences, Utrecht University, Padualaan 8, Utrecht
19 3584 CH, The Netherlands.

20 ⁶Hepatology Program, CIMA, CCUN, University of Navarra, Pamplona 31009, Spain;
21 CIBERehd, Instituto de Salud Carlos III, Madrid 28029, Spain.

22 ⁷Leibniz Institute for Analytical Sciences, ISAS e.V., Dortmund 44139, Germany.

23 ⁸Department of Gastroenterology, Hepatopancreatology and Digestive Oncology, Hôpital
24 Universitaire de Bruxelles, Université libre de Bruxelles, Brussels B-1070, Belgium.

25 ⁹Laboratory of Experimental Gastroenterology, Université libre de Bruxelles, Brussels B-
26 1070, Belgium.

27 ¹⁰Institute for Regeneration and Repair, Centre for Regenerative Medicine, University of
28 Edinburgh, Edinburgh EH16 4UU, United Kingdom.

29 ¹¹Instituto de Investigación, Desarrollo e Innovación en Biotecnología Sanitaria de Elche
30 (IDIBE), Av. de la Universidad s/n, Elche 03202, Spain.

31 ¹²IRIBHM, Université libre de Bruxelles, Brussels B-1070, Belgium.

32 ¹³Signalling Programme, Babraham Institute, Babraham Research Campus, Cambridge CB22
33 3AT, United Kingdom.

34 ¹⁴Singapore Immunology Network (SIgN), Agency for Science, Technology and Research
35 (A*STAR), 8A Biomedical Grove, Immunos, Singapore 138648, Singapore.

36 ¹⁵Department of Pharmacy, National University of Singapore, Singapore 117543, Singapore.

37 ¹⁶WELBIO Department, WEL Research Institute, Avenue Pasteur 6, Wavre B-1300, Belgium.

38

39 Running Title: PTPRK regulates hepatic glycolysis and lipid metabolism.

40

41 Corresponding author: Dr Esteban N. Gurzov
42 Signal Transduction and Metabolism Laboratory
43 Route de Lennik 808
44 Brussels B-1070
45 Phone: +32 2 555 8908
46 Email: esteban.gurzov@ulb.be

47

48 **Abstract**

49 Fat accumulation, *de novo* lipogenesis, and glycolysis are key drivers of hepatocyte
50 reprogramming and the consequent metabolic dysfunction-associated steatotic liver disease
51 (MASLD). Here we report that obesity leads to dysregulated expression of hepatic protein-
52 tyrosine phosphatases (PTPs). PTPRK was found to be increased in steatotic hepatocytes in
53 both humans and mice, and positively correlated with PPAR γ -induced lipogenic signalling.
54 High-fat-fed PTPRK knockout mice displayed reduced weight gain and hepatic fat
55 accumulation. Phosphoproteomic analysis in primary hepatocytes and hepatic metabolomics
56 identified fructose-1,6-bisphosphatase 1 and glycolysis as PTPRK targets in metabolic
57 reprogramming. Silencing PTPRK in hepatoma cell lines resulted in reduced colony-forming
58 ability and PTPRK knockout mice developed smaller tumours after diethylnitrosamine-
59 induced hepatocarcinogenesis. Our study defines a novel role for PTPRK in regulating hepatic
60 glycolysis, lipid metabolism, and tumour development. PTPRK inhibition may provide
61 therapeutic possibilities in obesity-associated liver diseases.

62

63

64

65

66

67

68

69

70

71

72

73

74 **Highlights**

- 75 • Hepatic receptor-type PTPs are increased in MASLD
- 76 • PTPRK is expressed in hepatocytes and upregulated in obesity
- 77 • PTPRK deficiency reduces body fat mass and liver steatosis in diet-induced obesity
- 78 • PTPRK regulates hepatic glycolysis and lipogenesis, promoting tumorigenesis

79

80

81

82

83

84

85

86

87

88

89

90

91

92

93

94

95

96

97

98

99 **Introduction**

100 Consumption of processed industrialized foods with high caloric density and reduced
101 energy expenditure results in nutrient overload. In response, cells adapt by storing energy in
102 the form of triglycerides, generating adipose tissue expansion and ectopic fat deposition in
103 organs such as the liver. The presence of a lipid-rich environment has deleterious pathological
104 consequences, including insulin resistance and dyslipidaemia. If not resolved, it can
105 evolve into non-alcoholic fatty liver disease (NAFLD), recently renamed metabolic
106 dysfunction-associated steatotic liver disease (MASLD), affecting a quarter of the global adult
107 population^{1,2}. Non-alcoholic steatohepatitis (NASH), a severe necro-inflammatory form of
108 NAFLD/MASLD, poses a significant health problem^{3,4}. Moreover, NAFLD/MASLD has
109 emerged as a leading cause of hepatocellular carcinoma (HCC), a highly heterogeneous and
110 aggressive malignancy⁵.

111 The liver is central to nutrient sensing and has a significant impact during obesity,
112 resulting in abnormal lipid accumulation and hepatocyte metabolic reprogramming. This
113 involves the intricate reorganization of anabolic and catabolic processes, all under the
114 transcriptional control of nutrient-sensitive receptors. In the context of obesity and HCC,
115 several transcription factors, including PPARs, SREBP1c, ChREBP, and HIF, participate
116 in the reshaping of metabolic pathways^{3,4}. In addition, post-translational modifications,
117 including phosphorylation of protein tyrosine residues, are dysregulated in nutrient overload
118 and obesity⁶.

119 Hepatic expression of Protein Tyrosine Phosphatases (PTPs) is affected in steatotic
120 livers and NASH. PTPs were conventionally perceived as enzymes responsible for
121 terminating or modulating signals initiated by tyrosine kinases⁷. Accumulating evidence
122 reveals their potential as signal propagators^{6,8}. For example, PTPN2 facilitates signalling

123 through both STAT1 and STAT3, exerting distinct influences on NASH and HCC⁹. Oxidative
124 inactivation of PTPN2 induces an insulin-STAT5-IGF-1-growth hormone pathway in
125 conditions of selective insulin resistance, contributing to obesity¹⁰. Receptor-type PTPs
126 (RPTPs) are transmembrane enzymes adapted to sense and transduce extracellular cues into
127 intracellular catalytic events¹¹. In obesity, inflammatory signals induce the expression of
128 PTPRG in the liver¹². Deleting or overexpressing PTPRG enhances or suppresses hepatic
129 insulin sensitivity, respectively¹². However, a lack of comprehensive studies to understand
130 liver PTPomes in obesity means that the role of PTPs in regulatory mechanisms and their
131 potential use as biomarkers or therapeutic targets remain largely unexplored.

132 PTPRK is a transmembrane receptor belonging to the R2B subfamily of RPTPs,
133 known to engage in homophilic interactions and localises to cell-cell contacts¹¹. Cell adhesion
134 proteins have been proposed as PTPRK substrates, and accumulating data associate PTPRK
135 with several human diseases¹³⁻¹⁵. The regulation of PTPRK involves a proteolytic cascade
136 (furin, ADAM10, and γ -secretase), potentially releasing the intracellular catalytic domain to
137 interact and dephosphorylate proteins in the cytoplasm or nucleus¹⁶. PTPRK is
138 transcriptionally regulated by transforming growth factor- β (TGF- β) and Notch signalling¹⁷.
139 Despite its potential in cell signalling, the downstream events regulated by PTPRK remain
140 unknown. In this study, we demonstrated that PTPRK is upregulated in fatty hepatocytes and
141 investigated its role in obesity-associated liver dysfunction. PTPRK deficiency leads to severe
142 metabolic changes in hepatocytes, culminating in reduced diet-induced obesity and hepatic fat
143 accumulation in mice. We identified fructose-1,6-bisphosphatase 1 (FBP1), a gluconeogenic
144 enzyme, as PTPRK target, bearing significant implications for glucose metabolism and liver
145 tumour growth. These findings underscore the pivotal role of PTPRK as key driver in the
146 metabolic reprogramming of hepatocytes induced by obesity.

147 **Results**

148 *Hepatic PTP expression is dysregulated in obesity-associated liver dysfunction*

149 The presence and potential contribution of PTP expression in the progression to
150 NAFLD/MASLD in obesity and the development of HCC remains unknown. Therefore, we
151 conducted a comprehensive analysis of the complete proteome and PTP expression patterns,
152 using liquid chromatography-tandem mass spectrometry (LC-MS/MS) analysis of human
153 liver samples (**Fig. 1A**). The cohort included liver biopsies obtained from individuals
154 exhibiting varying degrees of liver disease, encompassing simple steatosis (Metabolic
155 Associated Fatty Liver (MAFL)), NASH, HCC, and control samples from individuals without
156 evidence of liver damage (healthy liver). The heatmap illustrating the total proteome
157 alterations showed variations in protein expression and sample heterogeneity across different
158 stages of liver dysfunction (**Supplementary Fig. 1A**). KEGG pathway analyses revealed that
159 several protein modifications are related to metabolic dynamics. When comparing steatosis
160 with healthy livers, we observed activation of oxidative phosphorylation, starch, and sucrose
161 metabolism. We also observed activation of glutathione metabolism, alongside the
162 suppression of the tight junction pathway (**Supplementary Fig. 1B**). Activated pathways in
163 NASH included ECM receptor interaction, oxidative phosphorylation, and focal adhesion
164 (**Supplementary Fig. 1C**). Conversely, pathways related to the pentose phosphate pathway
165 (PPP), purine metabolism, histidine metabolism, and cysteine and methionine metabolism
166 were suppressed. Further, comparing NASH to steatosis, oxidative phosphorylation was
167 suppressed in NASH, while ECM receptor interaction, focal adhesion, and ribosome pathways
168 were activated (**Supplementary Fig. 1D**). Proteome analysis revealed key enzymes involved
169 in fatty acid uptake and metabolism, CD36, CPT1, and SCD, upregulated in steatosis and
170 NASH samples (**Fig. 1B**). Among the samples, 18 out of the 37 human PTP proteins were
171 identified (**Fig. 1C**). Analysis of the PTPome revealed that samples within the same disease
172 stage displayed similar PTP expression patterns (**Fig. 1D**), while analysis of RPTPs and non-

173 receptor protein tyrosine phosphatases (PTPNs) revealed opposing patterns across the stages
174 of the disease (**Fig. 1E**). Several PTPNs were downregulated with disease, while RPTPs
175 generally exhibited low expression levels in healthy liver samples but showed a marked
176 upregulation in steatosis and NASH. Specifically, PTPRK, PTPRE, PTPRM, PTPRF, and
177 PTPRA were elevated in steatosis and NASH (**Fig. 1F**). Single-cell RNA sequencing of
178 healthy-obese livers¹⁸ revealed that PTPRK is the most abundant RPTP in hepatocytes,
179 followed by PTPRG and PTPRM, with PTPRE mainly found in dendritic cells (**Fig. 1G**,
180 **Supplementary Fig. 1E**). Additionally, RPTP displayed comparable mRNA patterns in the
181 E-MEXP-3291 dataset (**Fig. 1H**). Correlation analysis showed that hepatic PTPRK, PTPRG,
182 and PTPRE transcript levels positively correlate with PPAR γ (**Fig. 1I**), a master regulator of
183 lipid accumulation in hepatocytes. Immunohistochemistry (IHC) analyses in human liver
184 samples showed that PTPRK levels were higher in steatosis and NASH, whereas healthy liver
185 displayed relatively lower expression. The PTPRK intracellular domain localised within
186 various cellular regions, including the nucleus of steatotic hepatocytes (**Fig. 1J**). The striking
187 remodelling of PTPomes with disease onset indicates a potential causative role in fat
188 accumulation and liver dysfunction.

189 *Hepatocyte PTPRK is induced in obesity and positively correlates with PPAR γ in mouse*
190 *models and primary hepatocytes*

191 To gain functional insights into the hepatic role of PTPRK we took advantage of
192 obesogenic mouse models. C57BL/6N mice were exposed to diet-induced obesity over a 12-
193 week period. Both high-fat diet (HFD) and high-fat, high-fructose high-cholesterol diet
194 (HFHFHCD) resulted in a noticeable increase in body weight (**Fig. 2A**), primarily attributed
195 to increased body fat mass (**Fig. 2B**). This was accompanied by elevated fasting insulin levels
196 (**Fig. 2C**), glucose intolerance (**Fig. 2D**), and reduced insulin sensitivity (**Fig. 2E**). PTPRK is
197 expressed in hepatocytes, but undetectable in subcutaneous and visceral adipose tissues or

198 muscle (**Fig. 2F**). Mice fed with HFHFHCD exhibited a greater liver weight, liver-to-body
199 weight ratio, and liver fat mass compared to the control group (**Fig. 2G,H**), consistent with a
200 more advanced stage of fatty liver development. PTPRK protein expression is enhanced in
201 HFD and HFHFHCD-fed mice livers, accompanied by PPAR γ upregulation (**Fig. 2I**). In line
202 with these results, adenovirus-mediated overexpression of PTPRK in mouse livers resulted in
203 a concomitant increase in PPAR γ levels (**Fig. 2J**). These results demonstrate a consistent
204 involvement of PTPRK in lipid metabolism and diet-induced liver dysfunction.

205 Extended culture of primary mouse hepatocytes resulted in a loss of differentiation,
206 causing changes in metabolic pathways similar to those observed *in vivo* during the
207 progression of NAFLD/MASLD. We observed a gradual accumulation of lipid droplets in the
208 cytosol of hepatocytes (**Fig. 2K**). This was accompanied with increased protein levels of
209 PTPRK and PPAR γ (**Fig. 2L**). Acute and chronic treatment of primary hepatocytes with
210 insulin or pro-inflammatory cytokines TNF α , IL6 or IFN γ did not affect PTPRK expression
211 (**Supplementary Fig. 2A-D**). NOTCH2 is significantly increased in primary hepatocytes over
212 time in culture (**Supplementary Fig. 2E**), and the administration of the Notch signalling
213 inhibitor GSIXX effectively prevented upregulation of both PTPRK and PPAR γ in a dose-
214 dependent manner (**Fig. 2M**). Treatment with lipopolysaccharide (LPS) significantly
215 increased both PTPRK and PPAR γ transcripts and protein levels (**Fig. 2N,O**). Additionally,
216 primary mouse hepatocytes treated with dimethylxalylglycine (DMOG), an inhibitor of 2-
217 oxoglutarate-dependent dioxygenases, resulted in reduced PTPRK and PPAR γ expression
218 levels (**Fig. 2P**). Together, these experiments provided compelling evidence of a positive
219 correlation between PTPRK and PPAR γ in hepatocytes, which can be regulated by diverse
220 signalling pathways.

221 *PTPRK deletion protects against diet-induced obesity, insulin resistance, and hepatic*
222 *steatosis in mice*

223 To directly evaluate the metabolic relevance of PTPRK, we conducted loss-of-
224 function studies using 8-week-old *Ptprk*^{-/-} and *Ptprk*^{+/+} mice subjected to either an HFHFHCD
225 or a chow diet. PTPRK deficiency had minimal impact on body weight gain and fat
226 accumulation in chow-fed mice (**Supplementary Fig. 3A-D**). Glucose and insulin tolerance
227 tests performed at 8 weeks of age showed no differences between *Ptprk*^{-/-} and *Ptprk*^{+/+} mice
228 (**Supplementary Fig. 3E-H**). At 20 weeks, *Ptprk*^{-/-} mice showed improved glucose
229 homeostasis (**Supplementary Fig. 3I-L**). The intake of chow diet was not affected
230 (**Supplementary Fig. 3M,N**). After 12 weeks of HFHFHCD feeding, *Ptprk*^{+/+} mice developed
231 obesity, characterised by substantial increases in body weight, fat mass, circulating insulin
232 levels, homeostasis model assessment of insulin resistance (HOMA-IR), glucose intolerance
233 and insulin resistance (**Fig. 3A-H, Supplementary Fig. 4A,B**). Strikingly, *Ptprk*^{-/-} mice
234 displayed resistance to HFHFHCD-induced obesity, as their body weight, fat mass, circulating
235 insulin levels, HOMA-IR, glucose sensitivity and insulin resistance were all significantly
236 lower (**Fig. 3A-H**). This protective effect was particularly prominent in female mice.

237 Consistent with the metabolic analyses, PTPRK-deficient mice exhibited elevated
238 energy expenditure, specifically during the dark cycle (**Supplementary Fig. 4C**). *Ptprk*^{-/-} mice
239 also displayed increased VO₂ levels during the night, and the respiratory exchange ratio (RER)
240 showed a downward trend (**Supplementary Fig. 4C**). No significant disparities were noted
241 in ambulatory activity or food and water intake (**Supplementary Fig. 4C,D**). The analysis of
242 food intake over a span of 12 weeks revealed no disparities in males, but lower levels in female
243 *Ptprk*^{-/-} mice, resulting in lower cumulative energy intake (**Supplementary Fig. 4E,F**).
244 PTPRK deficiency did not result in altered lipid excretion through faeces (**Supplementary**
245 **Fig. 4G**), suggesting that the reduced weight observed in *Ptprk*^{-/-} mice is not related to changes
246 in intestinal fat absorption. *Ptprk*^{-/-} livers exhibited significantly higher induction of p-IR and
247 p-AKT compared to *Ptprk*^{+/+} mice in response to insulin (**Fig. 3I**). The phosphorylation levels

248 induced by insulin on IR and AKT displayed no discernible differences in primary hepatocytes
249 (**Supplementary Fig. 5A**), indicating that PTPRK does not directly affect IR phosphorylation.
250 We observed a significant reduction in hepatic lipid accumulation within the livers of *Ptprk*^{-/-}
251 mice (**Fig. 3J-O**). Collectively, these findings demonstrate that while PTPRK-deficiency
252 exerts minimal influence on normal development, it confers robust protection against diet-
253 induced obesity, steatosis, and insulin resistance.

254 ***PTPRK expression shapes nutrient-driven metabolic reprogramming in hepatocytes***

255 Having established that PTPRK plays a major metabolic role in obesity, we next
256 sought to define the lipogenic pathways affected in HFHFHCD-fed mice. Immunoblot
257 analysis showed that *Ptprk*^{-/-} mice exhibited lower levels of hepatic PPAR γ (**Fig. 4A, B**), while
258 no differences were observed in subcutaneous and visceral adipose tissues (**Fig. 4C,D and**
259 **Supplementary Fig. 5B,C**). We observed significantly reduced expression of Ppar γ 2
260 transcripts in *Ptprk*^{-/-} mice, while Ppar γ 1 was unaffected (**Fig. 4E**). Key lipogenic enzymes,
261 namely *Scd1*, *Acly*, *Acc*, and *Fasn* mRNA were downregulated in *Ptprk*^{-/-} mice (**Fig. 4E**).
262 Immunoblot analysis confirmed diminished levels of ACC and FASN in *Ptprk*^{-/-} mice (**Fig.**
263 **4A,B**). In addition, transcription factors governing fat metabolism, SREBP1c and ChREBP,
264 also exhibited decreased expression in *Ptprk*^{-/-} livers (**Fig. 4A,B**).

265 Next, we used adenoviral-mediated upregulation of PTPRK in four week high-fat fed
266 mice and observed a significant increase in hepatic PPAR γ expression following adenoviral
267 infection (**Fig. 4F**). Adenoviral PTPRK overexpression reverted the hepatic phenotype of
268 obese *Ptprk*^{-/-} mice, including increased liver weight, liver-to-body weight ratio, and liver fat
269 mass (**Fig. 4G**). Histological examination of liver sections and lipid measurements revealed
270 pronounced lipid deposition following PTPRK overexpression (**Fig. 4H**). These results
271 demonstrate that hepatic PTPRK overexpression effectively reverses key phenotypic

272 characteristics observed in PTPRK-deficient mice. Primary hepatocytes with reduced PTPRK
273 levels (heterozygous) or complete deletion (knockouts) showed reduced kinetics of STAT1
274 phosphorylation in response to IFN γ (**Supplementary Fig. 5D,E**). STAT1 and Activator
275 Protein 1 (AP-1) play a pivotal role in driving PPAR γ expression and lipid accumulation
276 within the liver^{19,20}. Notably, we observed significantly lower levels of c-Fos/AP-1 in *Ptprk*^{-/-}
277 livers (**Supplementary Fig. 5F**). Taken together, our results suggest that PTPRK acts
278 upstream of transcriptional regulators of *de novo* lipogenesis and lipid metabolism in obesity.

279 ***Phosphoproteomic analysis revealed FBP1 as a PTPRK substrate in hepatocytes during*** 280 ***steatosis***

281 To explore the mechanisms by which PTPRK inactivation in hepatocytes might drive
282 the development of steatosis, we performed unbiased transcriptome and proteomic analysis.
283 Hepatocytes were isolated and separated based on their fat content (**Fig. 5A**). Immunoblot
284 analysis of high-fat content hepatocytes further established the positive correlation between
285 PTPRK and PPAR γ (**Fig. 5B**). Steatotic PTPRK-deficient hepatocytes have reduced Cd36
286 expression, a crucial PPAR γ target in cellular fatty acid uptake (**Fig. 5C**). In contrast, Cpt1,
287 facilitating long-chain fatty acid transport for mitochondrial β -oxidation, displayed an
288 opposing pattern, with higher expression in *Ptprk*^{-/-} hepatocytes (**Fig. 5C**). We performed
289 RNA-Seq analysis in low/high fat *Ptprk*^{-/-} and *Ptprk*^{+/+} hepatocytes (**Supplementary Fig.**
290 **6A**). Volcano plot analysis revealed that the predominant significant differences occurred
291 among genes upregulated in low-fat hepatocytes compared to high-fat hepatocytes within the
292 same genotype (**Supplementary Fig. 6B,C**). In contrast, only a limited number of genes
293 exhibited significant transcriptional alterations resulting from PTPRK deletion in low-fat or
294 high-fat hepatocytes (**Supplementary Fig. 6D,E**). We also observed reduced PPAR
295 signalling in *Ptprk*^{-/-} hepatocytes (**Fig. 5D**). Comparison of low-fat to high-fat *Ptprk*^{+/+}
296 hepatocytes revealed enriched pathways, including cell adhesion molecules, MAPK

297 signalling, PI3K-AKT signalling, cytokine interaction, and chemokine signalling (**Fig. 5E**).
298 In *Ptprk*^{-/-} hepatocytes, the same comparison highlighted pathways including gap junction,
299 ECM receptor interaction, focal adhesion, cAMP signalling, PI3K-AKT signalling, and RAP1
300 signalling.

301 We next performed proteomics and phosphoproteomic analysis of hepatocytes with
302 high-fat content (**Supplementary Fig. 6F**). The Venn diagram illustrates that 1148 proteins
303 show modifications in both the phosphoproteomic and total proteome datasets. This suggests
304 an intricate relationship between these protein datasets, indicating regulatory mechanisms
305 acting at the translational level and post-translationally through phosphorylation
306 (**Supplementary Fig. 6F**). The heatmap displays diverse protein changes between *Ptprk*^{-/-} and
307 *Ptprk*^{+/+} hepatocytes (**Fig. 5F**), revealing their dynamic response. In *Ptprk*^{-/-} hepatocytes, an
308 upregulation of specific proteins has been observed, reflecting a complex interplay of
309 molecular events associated with altered mitochondrial function and redox balance, closely
310 linked to cellular metabolic reprogramming (**Fig. 5G**). Enriched pathways include
311 metabolism, phagosome, and biosynthesis of unsaturated fatty acids (**Fig. 5H**). PTPRK-
312 deficiency increases phosphorylated residues across various proteins (**Fig. 5I**). These changes
313 are associated with crucial pathways, including insulin signalling, mTOR pathway, AMPK
314 signalling, insulin resistance, glucagon signalling, adherens junctions, and biosynthesis of
315 amino acids (**Fig. 5J**).

316 A total of 2572 phosphosites were significantly upregulated in *Ptprk*^{-/-} hepatocytes
317 compared with 258 found at lower levels (**Supplementary Fig. 6G**). Phosphotyrosine
318 residues of CPSM (pY162), CH10 (pY76), WASL (pY253), GSTP1 (pY8), and FBP1
319 (pY265, pY216) were increased in *Ptprk*^{-/-} hepatocyte (**Fig. 5K**). The focussed analysis of
320 FBP1, a hepatic tumour suppressor²¹, revealed changes also at the positions pS273, pS248,
321 pY265, pY245 and pY216 in *Ptprk*^{-/-} steatotic hepatocytes (**Fig. 5L**). FBP1 is a key enzyme

322 active in gluconeogenesis and glucose homeostasis. Structural modelling highlights conserved
323 helical regions (**Fig. 5M**) that engage with the PTPRK D2 domain (**Fig. 5N**), placing
324 phosphorylated tyrosine residues near the PTPRK catalytic D1 domain. Computational
325 simulations confirmed PTPRK and tyrosine phosphorylated complex predictions with a range
326 of different assemblies (**Supplementary Fig. 7A-F**). Pervanadate-treated hepatocyte lysates,
327 combined with recombinant PTPRK intracellular domain (PTPRK-ICD), demonstrated FBP1
328 dephosphorylation (**Fig. 5O**). Liver analyses in female *Ptprk*^{-/-} mice following a 12-week
329 HFHFHCD showed higher pFBP1 (pY265) levels (**Supplementary Fig. 8A**). We analysed
330 glycolysis dynamics using HYlight, a biosensor designed to track real-time changes in
331 intracellular levels of the FBP1 substrate, fructose 1,6-bisphosphate²². We observed a
332 reduction in fructose 1,6-bisphosphate levels in *Ptprk*^{-/-} hepatocytes when stimulated with
333 glucose (**Fig. 5P**). Our results demonstrate the dynamic interplay between PTPRK and FBP1,
334 significantly impacting glucose metabolism.

335 *Deletion of PTPRK induces metabolic reprogramming in the liver during diet-induced* 336 *obesity*

337 To assess the importance of hepatic PTPRK in glycolytic control, we cultured primary
338 mouse hepatocytes after adenovirus-mediated PTPRK overexpression or silencing (**Fig. 6A**).
339 Glucose-starved hepatocytes overexpressing PTPRK displayed increased glycolytic activity.
340 This was evident in the extracellular acidification rates measured after acute glucose injection
341 and after oligomycin blockade of mitochondrial respiration (**Fig. 6B**). Elevated glycolysis
342 channels pyruvate towards acetyl-CoA synthesis, triggering *de novo* lipogenesis. Hepatocytes
343 with PTPRK overexpression exhibited increased lipid droplet accumulation (**Fig. 6C**). In
344 addition, lipid droplet accumulation occurred to a greater extent in PTPRK overexpressing
345 hepatocytes after fatty acid administration (**Fig. 6C**). Inhibition of glucose oxidation resulted
346 in decreased PPAR γ expression, while PTPRK was not affected (**Supplementary Fig. 8B**).

347 We next sought to validate our results in human hepatocytes. *PTPRK*^{-/-} and *PTPRK*^{+/+}
348 human embryonic stem cells (hESC) were differentiated into hepatocyte-like cells (HLCs,
349 **Supplementary Fig. 8C-E**). Deletion of PTPRK did not affect hESC hepatocyte
350 differentiation nor the ability of HLCs to produce and secrete albumin (**Supplementary Fig.**
351 **8C-E**). Similar to mouse hepatocytes, PTPRK-deficient HLCs exhibited a reduced glycolytic
352 rate following glucose stimulation (**Supplementary Fig. 8F**). Together, these observations
353 indicate that PTPRK leads to steatosis indirectly by stimulating glycolytic activity and directly
354 by accelerating fatty acid esterification and lipid droplet formation in response to fatty acids.

355 Liver metabolites from *Ptprk*^{-/-} and *Ptprk*^{+/+} mice fed HFHFHCD for 12 weeks were
356 quantified by mass spectrometry (**Fig. 6D**). *Ptprk*^{-/-} livers showed decreased levels of
357 dihydroxyacetone phosphate and glyceraldehyde-3-phosphate, with a corresponding
358 reduction in the lactate/pyruvate ratio. *Ptprk*^{-/-} livers displayed elevated α -ketoglutarate levels
359 and increased pyruvate. Despite elevated pyruvate levels, *Ptprk*^{-/-} livers exhibited reduced
360 concentrations of acetyl-CoA, and increased free coenzyme A compared to *Ptprk*^{+/+}. This
361 aligns with our findings of decreased levels of pyruvate dehydrogenase phosphatase in *Ptprk*^{-/-}
362 mice, while no differences were observed for pyruvate dehydrogenase kinase
363 (**Supplementary Fig. 8G**). PTPRK deficiency also led to heightened pentose phosphate
364 pathway (PPP) intermediates, particularly ribulose-5-phosphate and erythrose 4-phosphate
365 (**Fig. 6D**). Enhancing the flux through the PPP could reinforce essential production of
366 reducing equivalents, and increase oxidative stress management. Parallel to shifts in lactate-
367 to-pyruvate ratio, *Ptprk*^{-/-} livers unveiled elevated GSSG (**Fig. 6D**) and methionine sulfoxide
368 levels (**Supplementary Fig. 8H**), indicative of an oxidised environment. The ratio of the
369 classical redox indicators NAD⁺/NADH, NADP⁺/NADPH, and GSSG/GSH showed no
370 significant changes (**Supplementary Fig. 8I**), although the total levels of NADP⁺ were
371 significantly lower in *Ptprk*^{-/-} (**Fig. 6D**). No differences were found in phosphorylated adenine

372 nucleotides (ATP, ADP and AMP, **Supplementary Fig. 8J**) and amino acids
373 (**Supplementary Fig. 8K**). We observed heightened expression of Pck1, a pivotal
374 gluconeogenic driver, in *Ptprk*^{-/-} livers (**Fig. 6E**), consistent with lower glycolysis. *Ptprk*^{-/-}
375 female mice, subjected to a 12-week HFHFHCD obesogenic diet, exhibited elevated blood
376 glucose levels compared to *Ptprk*^{+/+} after pyruvate injection, supporting a shift to a more
377 gluconeogenic state upon PTPRK deletion (**Fig. 6F**). Taken together, PTPRK plays a crucial
378 role in controlling liver metabolism through the regulation of glycolytic intermediates and
379 altered lipid dynamics.

380 *PTPRK contributes to hepatocyte transformation in obesity-associated HCC*

381 Glycolytic and gluconeogenic proteins, including FBP1 (**Supplementary Fig. 9A**),
382 contribute to HCC development²¹. We observed a stratification pattern based on PTPRK
383 mRNA expression levels in human samples (**Fig. 7A**) that bifurcated into two distinct clusters:
384 one characterised by high PTPRK expression and the other marked by low PTPRK expression
385 (**Fig. 7B**). Normal liver samples uniformly exhibited low PTPRK expression, while in the
386 context of NASH, peritumour, and tumour conditions, high PTPRK expression was correlated
387 with elevated hepatic expression of glycolytic genes. The analysis of all liver samples and the
388 focused analysis of tumour samples revealed a positive correlation between elevated PTPRK
389 expression and hepatic expression of lipogenic genes (**Fig. 7B**). The enriched pathways
390 associated with elevated PTPRK expression in liver tumour samples, as defined through
391 KEGG pathway enrichment analysis, underscored the activation of fatty acid metabolism,
392 type 1 diabetes mellitus, glycolysis/gluconeogenesis, TCA cycle, primary bile acid
393 biosynthesis, biosynthesis of unsaturated fatty acids, PPAR signalling pathway, steroid
394 biosynthesis, and oxidative phosphorylation (**Fig. 7C**).

395 To investigate the implications of PTPRK deletion in the context of liver cancer,
396 diethylnitrosamine (DEN), a potent hepatocarcinogen, was administered by a single injection
397 into *Ptprk*^{-/-} and *Ptprk*^{+/+} mice at the age of two weeks. *Ptprk*^{-/-} male mice showed reduced
398 body fat accumulation, while *Ptprk*^{-/-} females exhibited diminished body weight and fat
399 accumulation at the end of the experimental timeline compared with *Ptprk*^{+/+} (**Fig. 7D,G**).
400 Livers from *Ptprk*^{-/-} male and female mice were smaller, with reduced absolute hepatic lipid
401 content, although the relative liver fat content was unaltered (**Fig. 7D,G**). PTPRK deficiency
402 did not affect DEN-mediated tumour formation (**Fig. 7E,H**). However, macroscopic
403 evaluation showed reduced tumour size in *Ptprk*^{-/-} females (**Fig. 7H**). This was confirmed by
404 histological analysis of liver sections, where *Ptprk*^{-/-} tumours exhibited significantly
405 diminished dimensions and reduced fat accumulation regardless of gender (**Fig. 7E,F and**
406 **7H,I**). In line with these findings, silencing of PTPRK using siRNA in HepG2, HLE, and
407 Huh6 cell lines (**Fig. 7J,K and Supplementary Fig. 9B**) led to a substantial attenuation of
408 colony-forming capacity. Overall, our experiments support an oncogenic role of PTPRK in
409 promoting rapid hepatic tumour growth.

410 Discussion

411 Modern diets and lifestyles pose a chronic challenge to the ancestral mechanisms
412 designed to control energy balance in humans. In the present study, we observed increased
413 expression of hepatic RPTPs in steatosis and NASH, suggesting an adaptive response. The
414 upregulation of PTPRK may serve as a part of a compensatory mechanism to mitigate the
415 impact of disrupted cell adhesion components and mechanotransduction in fat-loaded
416 hepatocytes. PTPRK seems to play a pivotal role in disease progression, influencing
417 glycolysis, *de novo* lipogenesis signalling, and associated metabolic pathways.

418 We demonstrated that the upregulation of hepatocyte PTPRK-PPAR γ correlates with
419 NOTCH2 activation and that the inhibition of Notch signalling suppresses PTPRK-PPAR γ
420 expression in hepatocytes^{17,23}. In addition, LPS boosts PTPRK-PPAR γ , while HIF2 α represses
421 it. These results suggest that inflammation and hypoxia influence PTPRK expression,
422 potentially contributing to the differences observed in human liver samples. The correlation
423 between elevated PTPRK expression and the activation of glycolytic and lipogenic genes is
424 consistent with the role played by PTPRK in regulating these metabolic pathways.

425 Obesogenic diets lead to hepatic PTPRK overexpression, and global PTPRK knockout
426 mice are resistant to diet-induced metabolic dysfunction. The absence of PTPRK resulted in
427 delayed onset of obesity and NAFLD/MASLD with suppression of nutrient-sensitive
428 transcription factors PPAR γ , SREBP1c, and ChREBP, relevant for metabolic
429 reprogramming^{24,25}. We found that PTPRK deletion leads to c-Fos downregulation and lower
430 STAT1 activation in response to IFN γ . Both c-Fos and STAT1 are known to promote PPAR γ
431 expression^{19,20}. Interestingly, we demonstrated that inhibition of glucose oxidation suppresses
432 PPAR γ expression in hepatocytes without altering PTPRK expression. Thus, PTPRK-induced
433 glycolysis can contribute to increased PPAR γ expression. Glucose oxidation provides the
434 energy, metabolites, and reducing agents necessary for the execution of *de novo* lipogenesis
435 and sustains a shift in fatty acid metabolism from a catabolic to an anabolic direction²⁶.
436 PTPRK deficiency results in lower expression of the PPAR γ target gene CD36, a long-chain
437 free fatty acid transporter that promotes the growth of HCC cells by increasing glycolysis²⁷.
438 In overnutrition, PTPRK mediates the shift towards glycolysis and fat storage. PTPRK
439 deletion also protected mice against insulin resistance and hyperinsulinemia after obesogenic
440 diet feeding. Hepatic PTPRK overexpression is sufficient to reverse the phenotype. Elevated
441 insulin levels, insulin resistance, and excessive fat accumulation in hepatocytes are key drivers

442 of metabolic reprogramming, fuelling the phenotypic changes necessary for malignant
443 transformation of hepatocytes^{4,28}.

444 In aerobic conditions, pyruvate and cytosolic NADH are readily oxidised in the
445 mitochondria. However, as mitochondrial energy production meets cellular energy demand,
446 counterregulatory mechanisms are activated to slow down the TCA cycle and mitochondrial
447 function²⁹. If the glycolytic activity remains active, an excessive supply of acetyl-CoA
448 originating from pyruvate may accumulate, along with increased pyruvate fermentation into
449 lactate³⁰. The accumulated acetyl-CoA is then converted to malonyl-CoA, serving as a
450 substrate for *de novo* lipogenesis and an allosteric inhibitor of CPT1 α ²⁶. We found that the
451 metabolic balance is regulated by PTPRK and favoured the conversion of pyruvate into acetyl-
452 CoA by the pyruvate dehydrogenase complex. Indeed, we observed PTPRK-dependent
453 increased lactate/pyruvate ratio, reduced PDHK1/PDP1 ratio, accumulation of acetyl-CoA,
454 and upregulation of ACC and FASN. All these factors collectively contribute to the increased
455 lipogenic capacity of PTPRK-expressing hepatocytes, ultimately resulting in higher steatosis.

456 Glycolytic and gluconeogenic rates are reciprocally regulated, and the suppression of
457 gluconeogenic reactions favours glycolysis. The involvement of PTPRK in hepatic glucose
458 metabolism is an important determinant of the metabolic phenotype of PTPRK knockout mice
459 and the outcome of liver tumour formation experiments. Discrepancies in the role of PTPRK
460 in tumour development and growth in extrahepatic tissues³¹ may be due to the PTPRK–FBP1
461 regulation and its hepatic role in gluconeogenesis. Our experiments revealed that pyruvate and
462 α -ketoglutarate are elevated in PTPRK knockout mice. α -ketoglutarate is a TCA cycle
463 metabolite, that can supply carbons for gluconeogenesis; however, its accumulation reduces
464 liver gluconeogenesis³² and is associated with cancer suppression mechanisms³³. The build-
465 up of these gluconeogenic substrates indicates that even with a higher gluconeogenic capacity,
466 the livers of PTPRK knockout mice still possess regulatory mechanisms to prevent

467 uncontrolled gluconeogenesis. In line with this interpretation, hyperglycaemia was not
468 observed in PTPRK knockout mice, but higher glucose production was found during the
469 pyruvate tolerance test, in which animals were fasted to stimulate gluconeogenesis.

470 Fat-loaded hepatocytes isolated from PTPRK knockout mice showed an accumulation
471 of phosphorylated FBP1, and real-time detection of the metabolite fructose 1,6-bisphosphate
472 in primary hepatocytes lacking PTPRK revealed lower levels after glucose stimulation. Lower
473 fructose 1,6-bisphosphate levels during glycolysis may also be a direct implication of the
474 FBP1 tyrosine phosphorylation status. Thus, the observed outcome implies a futile cycle
475 between FBP1 and PFK1 activities during glycolysis and optimised glucose production during
476 gluconeogenesis. The substrate cycling at this step of glycolysis leads to wasteful ATP
477 consumption³⁴, in agreement with the observed increased energy expenditure in PTPRK
478 knockout mice and the substantial disparities observed for fat accumulation despite minor
479 differences in food intake. Further research is needed to explore the precise implications of
480 tyrosine phosphorylation on FBP1. Additionally, it is crucial to identify the tyrosine kinases
481 responsible for phosphorylating FBP1 and to examine the potential role of substrate cycling
482 in glycolysis in maintaining energy homeostasis.

483 Besides PTPRK, several classical PTPs present promising therapeutic opportunities.
484 However, developing selective and bioavailable PTP inhibitors has proved challenging³⁵.
485 Recent studies have shown the effectiveness of competitive inhibitors for closely related
486 PTPN2 and PTPN1^{36,37}. RPTPs can additionally be inhibited by inducing their dimerization.
487 For example, antibodies targeting PTPRD ectodomains induce protein dimerization and
488 degradation, thereby suppressing PTPRD-dependent cell invasion in a metastatic breast
489 cancer cell line³⁸. Therapeutic options for end-stage liver diseases are limited³⁹. PTPRK
490 inhibitors may hold potential in high-expressing PTPRK livers, as an alternative or adjuvant
491 treatment for obesity-associated liver dysfunction.

492 In conclusion, PTPRK expression is increased in diseased human and mouse livers.
493 Elevated hepatic PTPRK expression triggers heightened glycolysis, culminating in the
494 activation of PPAR γ and the stimulation of *de novo* lipogenesis. In mice, genetic PTPRK
495 inhibition offers protection against the rapid development of liver dysfunction associated with
496 obesogenic diet. Therefore, PTPRK emerges as a dual role player – serving as a biomarker for
497 hepatic metabolic adaptations that influence the risk of metabolic liver disease and as a target
498 for the development of new therapies. Screening and stratification of patients with
499 NAFLD/MASLD based on hepatic PTPRK expression levels could guide therapeutic
500 decisions to attenuate metabolic dysfunction associated with obesity.

501 **Materials and Methods**

502 *Reagents*

503 Human insulin solution, sodium pyruvate, sodium palmitate, oleic acid, bovine serum
504 albumin, 2-deoxy-D-glucose, D-glucose, mannoheptulose, DMOG, and LPS were obtained
505 from Sigma-Aldrich. Recombinant murine IFN γ (315-05-100ug PeproTech), recombinant
506 human IL6 (206-IL-010, R&D Systems), insulin ProZinc (NDC 0010-4499-01, Boehringer
507 Ingelheim, Rhein, Germany) were used for *in vivo* experiments.

508 *Human samples*

509 We studied 19 biopsy specimens of patients undergoing a liver biopsy for medical
510 reasons. The clinical characteristics of these patients are shown in **Supplementary Table 1**.
511 Biopsies were collected after approval of the Hôpital Erasme Ethics Committee. Written
512 informed consent was obtained from each participant.

513 *Extraction of proteins from human liver biopsies, enrichment of PTPs, and proteomics* 514 *analysis*

515 Frozen human liver biopsies were subjected to disruption using beads beating and
516 sonication. Lysates were treated with lysis buffer containing 10% glycerol, 1% NP-40,
517 cOmpleteTMEDTA-free protease inhibitor cocktail (Roche Diagnostics), and 1× phosphatase
518 inhibitor (Sigma-Aldrich). After sonication, centrifugation at 20,000g for 1h at 4°C separated
519 insoluble debris, retaining the supernatant for total proteome analysis. The obtained lysates
520 were enzymatically digested using trypsin, targeting C-terminal lysine and arginine residues,
521 except when adjacent to a C-terminal proline. Purification of the resulting peptides was
522 performed using reverse-phase Sep-Pak C-18 cartridges, removing salts and buffers. By
523 employing a strategy that explores the oxidation of cysteine in the catalytic site of PTPs,
524 peptides containing cysteine residues within the PTP signature motif HCX5R were enriched
525 through immunoprecipitation. Immunoprecipitated peptides, resuspended in 0.2% formic
526 acid, were injected in triplicate for LC-MS/MS analysis. A 40-min reverse-phase gradient
527 separation on UHPLC 1290 (Agilent Technologies) was followed by analysis on an Orbitrap
528 Q Exactive HF mass spectrometer (Thermo Fisher Scientific), with MS scans spanning the
529 375–1500m/z range at 60,000 resolution. Data were acquired in Data-Dependent Acquisition
530 mode, selecting the top 7 precursor ions for HCD fragmentation, followed by MS/MS analysis
531 at 30,000 resolution. MaxQuant (version 2.0.3.0) processed spectral files, searching the Homo
532 sapiens Uniprot database with FDR restricted to 1%.

533 *Mice*

534 Mice were housed and managed in compliance with the Belgian Regulations for
535 Animal Care, and the animal protocols underwent approval from the Commission d’Ethique
536 du Bien-Être Animal (CEBEA), Faculté de Médecine, Université libre de Bruxelles (dossier
537 No. 732). Animals were housed at 22°C on a 12:12-h light-dark cycle with ad libitum access
538 to food and water. *Ptprk* knockout mice were generated at The Jackson Laboratory (*Ptprk*-
539 8356J-M669 project) by CRISPR/Cas9 technology and were bred on a pure C57BL/6N

540 background. The strategy involved an intragenic deletion spanning 555 base pairs on
541 Chromosome 10. This genetic alteration led to the excision of exon 3 within the *Ptprk* gene,
542 accompanied by the removal of 283 base pairs from adjacent intronic sequences. The resulting
543 mutation is predicted to induce an alteration in the amino acid sequence following residue 74
544 and an early truncation by 2 amino acids.

545 By breeding *Ptprk*^{+/-} mice we obtained *Ptprk*^{-/-} and *Ptprk*^{+/+} males and females
546 littermates. *Ptprk*^{+/+} and *Ptprk*^{-/-} mice, aged 8 weeks, were randomly assigned to experimental
547 diet-induced obesity feeding with unrestricted access to the specific diets: a HFD (60 kcal%
548 fat D09100310i), a HFHFHCD (40 kcal% Fat, 20 kcal% Fructose, and 2% Cholesterol,
549 D09100310i), or a control diet (10 kcal% Fat, D09100304i) from Research Diets (New
550 Brunswick, NJ, USA). The duration for which the animals were subjected to the experimental
551 diets ranged from 4 to 24 weeks, as indicated.

552 *Metabolic analysis*

553 Evaluation of body and liver lean and fat mass was performed with EchoMRI™ 3-in-
554 1 (NMR) body composition analyser from EchoMedical Systems (Houston, TX, USA).

555 Glucose tolerance tests were performed in 6h fasted mice with an intraperitoneal
556 administration of glucose (2g D-Glucose/kg body weight). For pyruvate tolerance tests, mice
557 were fasted overnight and administered pyruvate (2g/kg). Insulin tolerance tests were
558 performed on mice fasted for 4h, with an intraperitoneal injection of insulin (0.75U/kg body
559 weight). Fresh D-glucose, pyruvate, or insulin solutions were prepared in PBS immediately
560 before the injections. Blood samples were obtained from the tail tip, and glycemia was
561 measured using a glucometer (Accu-Check Performa, Roche, Basel, Switzerland). Blood
562 serum was collected in a fed state (9am) or 6h after fasting (3pm) and insulin levels measured
563 by ELISA (Crystal Chem Inc.).

564 At 18 weeks of age, *Ptprk*^{-/-} and *Ptprk*^{+/+} mice fed HFHFHCD for 10 weeks, were
565 placed in metabolic cages TSE Phenomaster setup (TSE, Germany) for a duration of 72h.
566 Following a 24h period of acclimatization, metabolic parameters, including physical activity,
567 energy expenditure, and substrate utilization were assessed by indirect calorimetry.

568 *DEN-induced HCC*

569 Liver tumour formation was induced by administering 25mg/kg of DEN in PBS via
570 intraperitoneal injection into the underbelly region of 14-day-old mice. The mice were
571 maintained on a chow diet. At 40 weeks of age, the mice were euthanized through cervical
572 dislocation, and their livers were extracted for comprehensive analysis, including macroscopic
573 and histological assessment of tumour number and size.

574 *Histological analysis*

575 Mouse liver tissues intended for histological analysis were collected from euthanized
576 mice, dissected, and subsequently rinsed with PBS. The tissues were fixed in 4% buffered
577 formaldehyde (pH 7.4), embedded in paraffin blocks, sectioned into slices measuring 5-7µm
578 using a Leica rotator microtome and stained with haematoxylin and eosin (H&E).

579 For immunohistochemistry analysis of PTPRK in human liver samples, 7µm thick
580 paraffin sections were situated on positively charged slides. Antigen unmasking was
581 performed with a heated citrate buffer (10mM, pH6.0). The sections were permeabilized using
582 triton (0.1%), subsequently blocked with 2% milk, and incubated with 10% normal goat serum
583 to prevent nonspecific binding. Primary antibodies were incubated overnight at 4°C, followed
584 by incubation with goat anti-rabbit horseradish peroxidase secondary antibody (P044801).
585 Negative controls were established by subjecting specimen slices solely to the secondary
586 antibody.

587 Lipid accumulation was assessed by Nile Red staining (Sigma-Aldrich N3013).
588 Primary hepatocytes were isolated and seeded onto chambered coverslips (IBIDI, 80806) at a
589 density of 50,000 cells per well, 4h before adenoviral transfection for either PTPRK
590 overexpression or silencing. After 24h of transfection, the culture medium was replaced with
591 BSA-conjugated free fatty acids (sodium palmitate 0.4mmol/L, oleic acid 0.8mmol/L) or free
592 fatty acid-free 1% BSA control-enriched medium with 1% FBS. The hepatocytes were fixed
593 in 4% formaldehyde solution for 20min and stained with a 5µg/mL Nile Red solution and the
594 nucleus were stained with DAPI. The stained cells were observed using an inverted
595 fluorescence microscope (Axio Observer D1, Carl Zeiss, Oberkochen, Germany). The same
596 staining procedure was applied to hepatocytes with high-fat and low-fat content, fixed and
597 stained following an overnight culture period.

598 Hepatic lipid content was assessed in frozen sections of both *Ptprk*^{+/+} and *Ptprk*^{-/-} livers
599 through Oil Red O (ORO) (Sigma-Aldrich, O1391) staining. Liver sections from cryostat cuts
600 were equilibrated for 30min at room temperature in laminar flow hood. ORO working solution
601 (0.3% ORO in 60% isopropanol) was applied to ensure complete coverage and incubated at
602 37°C. After counterstaining with haematoxylin, images were captured using NanoZoomer
603 Digital Pathology (Hamamatsu Photonics K.K., version SQ 1.0.9) at 40x magnification.

604 ***Lipid extraction***

605 Total hepatic lipid content was evaluated by gravimetry after lipid extraction. Livers
606 were removed, immediately freeze-clamped in liquid nitrogen, and stored at -80°C. The liver
607 samples (100mg) were homogenized using a bead tissue homogenizer with cold methanol.
608 After sonication, the homogenate was transferred to Falcon tubes. Chloroform was added, and
609 the mixture was vortexed. Following agitation overnight at 4°C, the samples were centrifuged
610 at 13,500g for 10min. The organic phase was collected, allowed to air-dry at room

611 temperature, and the resulting pellet was weighed for total fat quantification. The solid middle
612 layer formed during centrifugation was dried and weighed to determine the protein content.
613 The results were expressed as mg of fat/100g of liver and g of fat/g of protein in the liver.

614 *LC-MS analysis of glycolytic, tricarboxylic acid (TCA) cycle, and pentose phosphate*
615 *pathway (PPP) intermediates*

616 The metabolomics analysis was conducted at the VIB Metabolomics Core (Leuven,
617 Belgium). Polar metabolites were extracted using a two-phase methanol-water-chloroform
618 method⁴⁰. Dried metabolite samples were reconstituted in a solution of 60% acetonitrile and
619 then transferred to LC-MS vials. For the analysis, an UltiMate 3000 LC System (Thermo
620 Scientific) was coupled to a Q-Exactive Orbitrap mass spectrometer. Separation was achieved
621 using a SeQuant ZIC/ pHILIC Polymeric column (Merck Millipore). A gradient of solvent A
622 (95% acetonitrile-H₂O, 2 mM ammonium acetate pH 9.3) and solvent B (2 mM ammonium
623 acetate pH 9.3) was employed. Mass spectrometry was performed in the negative ion mode,
624 encompassing both full scans and a targeted Selected Ion Monitoring (SIM) approach. Data
625 acquisition was managed using Xcalibur software (Thermo Fisher Scientific)⁴¹. The data is
626 presented as raw abundances corrected for sample weight.

627 *Primary mouse hepatocyte isolation, cell culture and treatments*

628 Mouse primary hepatocytes were isolated from *Ptprk*^{-/-} and *Ptprk*^{+/+} mice following
629 overnight ad libitum feeding, utilizing a two-step collagenase perfusion method through the
630 vena cava. The process was initiated by anaesthetizing the mice through an intraperitoneal
631 injection of a ketamine (100mg/kg) and xylazine (10mg/kg) mixture, peritoneum was opened,
632 and the infra-hepatic segment of the vena cava was cannulated for perfusion. The portal vein
633 was cut to clear blood from the liver. In the first perfusion step, the liver was exposed to HBSS
634 (Thermo Fisher Scientific) supplemented with 10mM HEPES (pH 7.4), saturated with O₂/CO₂

635 (95:5 vol/vol), at 37 °C for 10min. The second step involved adding collagenase type IV
636 (0.3 mg/mL) to William's E Medium (Thermo Fisher Scientific) and further perfusing for
637 10min, effectively digesting the liver tissue. The digested liver was transferred to a sterile
638 plastic dish, and cells were dispersed using a coarse-toothed comb in cold William's E
639 Medium, followed by filtration through a 100- μ m cell filter to eliminate cell clumps. The
640 resulting clump-free cell suspension was pelleted through centrifugation at 50g for 5min at
641 4 °C, the pellet was resuspended in William's E Medium and layered onto Percoll[®] solution
642 (Sigma-Aldrich) (10ml Percoll[®] + 1.25ml PBS 10X + 1.25 ml H₂O.) and centrifuged for 10
643 min at 1000 RPM. The pellet was resuspended in William's E Medium and washed 3 times
644 (centrifugation at 50g for 5min at 4 °C). Viability assessment using the trypan blue exclusion
645 test yielded approximately 15-20 million cells with 85% viability.

646 Hepatocytes with high-fat and low-fat content were isolated from steatotic livers⁴².
647 Viable hepatocytes with different lipid contents were separated from dead hepatocytes and
648 non-parenchymal cell types in the cell suspension using Percoll[®] gradient and differential
649 centrifugation. The hepatocytes were resuspended, washed, and assessed for cell number and
650 viability using trypan blue and a hemacytometer and immediately plated for experiments or
651 pelleted and stored at -80°C for further RNA or protein extractions used in RNA-Seq and
652 proteomic/phosphoproteomic analyses.

653 HepG2, HLE, and Huh6 cell lines were cultured using DMEM with 10% heat-
654 inactivated FBS and Penicillin-Streptomycin. For mouse primary hepatocytes, 100,000
655 cells/well in a p24 plate using attachment medium (William's Medium with Glutamax, 10%
656 Foetal Bovine Serum (FBS), 1% Penicillin-Streptomycin, and 10 mM HEPES). After
657 attachment, the media was replaced with a maintenance medium (William's E Medium with
658 Glutamax, 10% FBS, 1% Penicillin-Streptomycin, 1% non-essential amino acids, 10mM

659 HEPES, and 5 μ M hydrocortisone). Cell death was measured using SYTOX green (Thermo
660 Fisher Scientific).

661 *LC-MS analysis of total proteome and phosphoproteome changes*

662 The cell pellets originating from primary hepatocytes were lysed in cold HEN Buffer
663 supplemented with PhosSTOP (Roche) and cOmplete™, EDTA-free Protease Inhibitor
664 Cocktail (Roche). Lysates were precipitated twice using methanol/chloroform precipitation
665 (Sample:Methanol:Chloroform, 4:4:1). Pellets were resuspended using 2% SDS in 50mM
666 HEPES, and protein concentration was performed using DC protein assay (Bio-Rad
667 Laboratories). An equal amount of protein was subjected to reduction and alkylation by
668 incubating the samples with 5mM DTT for 1h at 37°C, followed by incubation with 20mM
669 iodoacetamide at room temperature for 30min. Pellets were dissolved using 6M Guanidine-
670 HCl in digestion buffer (50mM ammonium bicarbonate, 1mM CaCl₂). 250 μ g of proteins were
671 diluted to 0.3M Guanidine-HCl in digestion buffer and digested using trypsin (protein:trypsin,
672 20:1, w/w). Peptides were desalted on Supel™-Select HLB SPE Tube (Sigma-Aldrich).
673 Eluates were evaporated under a vacuum until dryness. Peptides were dissolved in 80%
674 acetonitrile and 0.1% TFA. Before enrichment, digestion quality control was performed using
675 an Ultimate 3000 Nano Ultra High-Pressure Chromatography system with a PepSwift
676 Monolithic® Trap 200 μ m*5mm (Thermo Fisher Scientific). One part of the sample was kept
677 aside and dried again for total proteomic analysis. The phosphorylated peptides enrichment
678 was performed using Fe(III)-NTAcartridges (Agilent Technologies) using the AssayMAP
679 Bravo Platform (Agilent Technologies)⁴³. Cartridges were primed and equilibrated with 0.1%
680 TFA in ACN and 0.1% TFA, 80% ACN (loading buffer) solutions, respectively. Cartridges
681 were then washed with loading buffer and eluted using 1% NH₄OH. Peptides were
682 immediately acidified using 10% formic acid (FA) and dried in vacuum. Both total proteome
683 and phosphoproteome were analysed by high-resolution LC-MS/MS using an Ultimate 3000

684 Nano Ultra High-Pressure Chromatography system (Thermo Fisher Scientific) coupled with
685 an Orbitrap Eclipse™ Tribrid™ Mass Spectrometer via an EASY-spray (Thermo Fisher
686 Scientific). For the total proteome analysis, peptide separation was carried out with an
687 Acclaim™ PepMap™ 100 C18 column (Thermo Fisher Scientific) using a 155min linear
688 gradient from 3 to 35% of B (84% ACN, 0.1% FA) at a flow rate of 250nL/min. The peptide
689 separation for the phosphoproteome analysis was carried out with an Acclaim™ PepMap™
690 100 C18 column (Thermo Fisher Scientific) using a 155min non-linear gradient from 3 to 35%
691 of B (0 min, 3% B; 135min, 30% B; 155min, 42% B; B:84% ACN, 0.1% FA) at a flow rate
692 of 250nL/min. Both were analysed using the Orbitrap Eclipse™ operated in a DDA mode.
693 MS1 survey scans were acquired from 300 to 1,500m/z at a resolution 120,000 using the
694 Orbitrap mode. MS2 scans were carried with high-energy collision-induced dissociation
695 (HCD) at 32% using the Normal speed IonTrap mode. Data were evaluated with Proteome
696 Discoverer software using 10ppm for precursor mass tolerance, 0.5Da for the fragment mass
697 tolerance, specific tryptic digest, and a maximum of 3 missed cleavages.
698 Carbamidomethylation (+57.021464Da) on C was added as a fixed modification. N-term
699 Acetylation (+42.010565Da) and methionine oxidation (+15.994915Da) were added as
700 variable modifications. Phosphorylation (+79.966331) on S, T, and Y was added as variable
701 modification only for the phospho-proteome analysis in addition to other mentioned
702 modifications. Peptide-spectrum matches and proteins were filtered at FDR 1%. Protein
703 abundancies (total proteome) were normalized using TIC. Phosphorylated peptide
704 abundancies were normalized using eigenMS⁴⁴ with R studio.

705 *Adenoviral infection*

706 Adenoviral-mediated hepatic PTPRK overexpression was performed by retro-orbital
707 injection of 1.8×10^9 PFU (Ad-*Ptpk*, construct Ad-m-PTPRK, SKU: ADV-269821) in 200μL
708 of PBS, and Adv-CMV-Null was used as control (Ad-control, #1300).

709 In primary mouse hepatocytes, we used adenoviral vectors to achieve PTPRK
710 overexpression (Ad-*Ptprk*, construct Ad-m-PTPRK, SKU: ADV-269821) and silencing (Ad-
711 shRNA *Ptprk*, construct Ad-GFP-U6-m-PTPRK-shRNA, SKU: shADV-269821). The cells
712 were used for the experiments 48h after the exposure to the vectors. The vectors were obtained
713 from Vector Biolabs.

714 *In vitro RNA interference and colony formation assay*

715 To induce PTPRK knockdown, we transfected HepG2, HLE, and Huh6 cell lines with
716 siRNAs targeting PTPRK or a negative control siRNA (working concentration 30nmol/L;
717 QIAGEN). The delivery of siRNA was achieved using Lipofectamine™ RNAiMAX
718 Transfection Reagent (Thermo Fisher Scientific) in Opti-MEM™ I Reduced Serum Medium
719 (Thermo Fisher Scientific). The siRNA target sequences are detailed in **Supplementary**
720 **Table 2**.

721 48-h after siRNA transfection, the cells underwent trypsinization to attain a single-cell
722 suspension. For the colony formation assays, 2,000 cells were seeded into P6 plates. After 1-
723 2 weeks, depending on the specific cell line, the resultant colonies were fixed with 4% PFA
724 solution and staining with 0.5% crystal violet.

725 *Dephosphorylation assay*

726 The dephosphorylation assay employed pTyr-enriched lysates obtained from primary
727 mouse hepatocytes treated with pervanadate¹³. The hepatocytes were incubated with a
728 recombinant PTPRK intracellular domain (PTPRK-ICD, 150nM final concentration). The
729 reaction was stopped after 90-min using SDS, and the resulting samples were subjected to
730 immunoblot analysis of phospho-FBP1 (pY265).

731 *Extracellular acidification rates measurement during glycolytic stress test*

732 Glycolytic rates were evaluated using the XFp Flux Analyzer from Seahorse
733 Bioscience (Agilent Technologies). Primary hepatocytes were plated in the Seahorse plates
734 (10,000 cells/well). After attachment and adenoviral treatments, the cells were allowed to
735 equilibrate in XF Base media (glucose-free, Seahorse Bioscience) supplemented with 2mM
736 glutamine at 37°C for 1h in a CO₂-depleted incubator. The XF Base media was refreshed again
737 immediately before starting the ECAR measurements. The glycolytic stress test was
738 conducted adding glucose (10mM), oligomycin (10μM), and 2-DG (100mM, divided into two
739 consecutive injections of 50mM). After the test, the medium was removed, and the cells were
740 immediately collected in 50μl of cell lysis buffer (Cell Signaling Technology) supplemented
741 with Halt protease and phosphatase inhibitor cocktail (Thermo Fisher Scientific). The cells
742 were stored at -80°C for posterior protein measurements and immunoblot analysis.

743 *Western blotting*

744 RIPA buffer (Cell Signaling Technology) was used to extract total protein lysates from
745 tissues, while cell total protein lysates were prepared using Cell Lysis Buffer (Cell Signaling
746 Technology). Both lysis buffers were supplemented with Halt protease and phosphatase
747 inhibitor cocktail (Thermo Fisher Scientific). Protein quantification was performed using a
748 BCA protein assay kit (Thermo Fisher Scientific). Separated by polyacrylamide gels, 20–50μg
749 of protein lysate was subsequently transferred to a 0.22μM nitrocellulose membrane (Bio-Rad
750 Laboratories). Primary antibodies (**Supplementary Table 3**) were diluted in milk-blocking
751 buffer. Detection of proteins employed goat anti-rabbit IgG (Dako Agilent), goat anti-mouse
752 IgG (Dako Agilent), and Peroxidase AffiniPure Donkey Anti-Human IgG (Jackson
753 ImmunoResearch) secondary antibodies. Immunoreactive bands were detected using a
754 Western blot imaging system (Amersham ImageQuant 800 Western blot imaging system,
755 Cytiva Life Science).

756 *RNA extraction, qPCR, and transcriptomics analysis*

757 Poly(A)⁺ mRNA extraction was performed with Dynabeads™ mRNA DIRECT™
758 Purification Kit (Thermo Fisher Scientific). Reverse transcription was carried out with a
759 reverse transcriptase kit (Eurogentec). Quantitative real-time PCR was performed using a Bio-
760 Rad CFX (Bio-Rad Laboratories) and SYBR Green reagents (Bio-Rad Laboratories). Probe
761 and primer details can be found in **Supplementary Table 4**. For tissues or isolated
762 hepatocytes with high-fat and low-fat content the total RNA was obtained using a RNeasy
763 Mini Kit (QIAGEN) following the manufacturer's instructions. cDNA synthesis and qPCR
764 were performed as described above. For the transcriptomics experiments, total RNA quality
765 analysis, library preparation, and sequencing were performed by the BRIGHTcore facility
766 (Brussels, Belgium). Sequencing was performed on an Illumina NovaSeq 600. An average of
767 25 million paired-end reads of 100 nucleotides were obtained per sample. The list of up-
768 /downregulated genes/transcripts and association with canonical pathways were determined
769 with the use of the online Degust software with Limma/Voom and packages Bioconductor
770 EGSEA and ComplexHeatmap in RStudio.

771 *Bioinformatic analysis*

772 For the comparative analysis among healthy, steatosis and NASH conditions, the
773 Kruskal-Wallis test was employed. The comparison analysis was conducted on mRNA
774 expression data from the publicly available E-MEXP-3291 study, and the analysis was
775 executed using R (version 4.2.2). The correlation analysis focused on investigating the
776 relationship between Ppar mRNA (x-axis) and RPTPs mRNA (y-axis) using the Pearson
777 correlation method. The data was obtained from the publicly available E-GEOD-48452 study.
778 The analysis was performed in R (version R 4.2.2). To assess the statistical significance of the
779 correlation, a significance level ($p < 0.05$) was set, and p-values were calculated. To study the

780 expression of RPTPs in human liver, single-cell RNA-Seq dataset of human healthy-obese
781 livers was obtained from¹⁸. The dataset along with cell annotations were downloaded from
782 Gene Expression Omnibus (GEO), accession number GSE192740. Using the information
783 provided by the authors, the UMAP and gene expression were plotted using Seurat⁴⁵. Publicly
784 available transcriptomic data (RNA-seq) corresponding to GSE164760 was downloaded from
785 the NCBI Sequence Read Archive (SRA) in fastq format using version 3.0.0 of the *SRA*
786 *Toolkit*. Adapter sequences were removed using *TrimGalore* version 0.6.0
787 with *Cutadapt* version 1.18⁴⁶. The clean reads were aligned to the reference genome using the
788 splice-aware aligner *STAR* version 020201⁴⁷ based on the hg38 genome version. The aligned
789 reads were quantified using *HTseq* version 0.11.0. The trimmed mean of M values method
790 was used with *EdgeR* version 3.28.1⁴⁸, R software (version 3.6.3).

791 Heatmap visualization was carried out with *ComplexHeatmap* R package and all
792 samples were referred to the mean of the control groups, log₂ transformed with trimmed
793 standard deviation in proteomic and transcriptomic databases.

794 ***Measurement of fructose 1,6-bisphosphate in cells using HYlight***

795 The HYlight biosensor²² responds to changes in fructose 1,6-bisphosphate levels. Cells
796 were transfected with the pCS2+_HYlight plasmid²² using Lipofectamine 3000
797 (ThermoFisher). 1h before imaging, cells were subjected to glucose starvation using XF assay
798 medium. Live-cell imaging was conducted on a Nikon AX confocal system and a 20X
799 objective (NA 0.8, Plan Apo λD 20x OFN 25 DIC N2) with the perfect focus system (PFS).
800 The transfected cells were excited at 488nm and 405nm, and emission was captured using a
801 525/25nm emission filter. Imaging was performed at 37°C. Image processing was performed
802 with NIS-Elements software (Nikon), single-cell regions of interest (ROIs) were manually
803 selected. The excitation ratio $F_{488/405}$ was measured for each ROI over time.

804 ***PTP activity assay***

805 Recombinant PTPRK intracellular domain (PTPRK ICD) was purified¹³, and the
806 pNPP phosphatase activity assay was conducted as previously described⁴⁹. PTP was buffer
807 exchanged to the activity assay buffer (20mM HEPES, 100mM NaCl, pH 7.4) using an
808 Amicon 10kDa MWCO. The assay buffer was degassed by flushing with Argon. PTP was
809 subjected to the indicated treatments (inhibitors or vehicle) and loaded into a 96-well plate.
810 The reaction was initiated by the addition of 15mM or the indicated concentrations of pNPP
811 to the reaction mixture. To determine the IC₅₀ value, the reactions were prepared by adding
812 the inhibitor or DMSO to a reaction mixture containing PTP, incubating at room temperature
813 for 5 min, and centrifuged at 14,000 rpm. The supernatant was transferred to a 96-well plate.
814 The reaction was initiated by the addition of 30mM pNPP to the reaction mixture. The
815 formation of p-nitrophenol was measured at absorbance of 405nm at 27°C on an ID5
816 spectrometer. Initial velocity (V₀) was determined using linear regression in GraphPad Prism.

817 ***Stem cell differentiation into HLCs***

818 The differentiation of CRISPR/Cas12-edited hESC H1 (WiCell) into HLCs followed
819 the protocol previously described⁵⁰. Laminin-coated plates were prepared and stem cells were
820 detached, seeded into the laminin-coated plates, and allowed to reach optimal confluency
821 before differentiation. Albumin was measured in the cell culture medium by Human
822 ALB/Serum albumin ELISA Kit (Sigma-Aldrich) and in the cell lysate by qPCR. The
823 differentiated cells were used for glycolytic stress tests.

824 ***Statistical analysis***

825 The results are presented as the mean ± standard error of the mean (SEM). Student's
826 t-test was used for comparisons between two groups. Differences among groups were assessed

827 by two-way ANOVA or repeated-measures ANOVA. Statistical analyses were assessed using
828 Prism software (GraphPad Software, Inc, La Jolla, CA, USA). Sample size was predetermined
829 based on the variability observed in prior experiments and on preliminary data. Differences
830 were regarded as statistically significant if $*p < 0.05$; $**p < 0.01$; $***p < 0.001$.

831 ***Data and Resource Availability***

832 The RNA-Seq dataset generated during the sequencing procedure is deposited in
833 the Gene Expression Omnibus database (access number GSE247670), the mass spectrometry
834 proteomics and peptidomics datasets have been deposited to the ProteomeXchange
835 Consortium via the PRIDE partner repository (access numbers PXD046949, PXD46506) and
836 available from the corresponding author upon reasonable request.

837 ***Financial support:*** This work was supported by a European Research Council (ERC)
838 Consolidator grant METAPTPs (Grant Agreement No. GA817940), FNRS-WELBIO grant
839 (35112672), FNRS-PDR grant (40007740), FNRS-TELEVIE grant (40007402), and ULB
840 Foundation. The Ministry of Science and Innovation, through its State Plan for Scientific,
841 Technical and Innovation Research (Project PID2021-125188OB-C32) and the Generalitat
842 Valenciana (PROMETEO/2021/059) supported the work in the Encinar laboratory. MRF is
843 funded by European Research Council (ERC) under the European Union's Horizon 2020
844 research and innovation programme (Grant Agreement No. 864921). JM is supported by a
845 VIB grant. ENG is a Research Associate of the FNRS, Belgium.

846 ***Acknowledgements:*** We thank André Dias, Madalina Popa, Erick Arroba, Mariana Nunes,
847 Francisco Costa, Anne Van Praet, Anaïs Schaschkow (Université libre de Bruxelles) for
848 experimental and technical support, Nicolas Baeyens (Université libre de Bruxelles) for live-
849 imaging microscopy advice, John Koberstein (Howard Hughes Medical Institute) for the
850 HYlight biosensor, Carlos Martinez-Cáceres (IMIB) for pathological analysis of the samples,

851 the Consortium des Équipements de Calcul Intensif (CÉCI) for the computer cluster NIC5,
852 and Hercules2 for providing computing facilities. We thank Cédric Blanpain (Université libre
853 de Bruxelles), Sarah-Maria Fendt (KULeuven) and Latifa Bakiri (Medical University of
854 Vienna) for critical reading of the manuscript.

855 **References:**

856

857 1 Rinella, M. E. *et al.* A multi-society Delphi consensus statement on new fatty liver disease
858 nomenclature. *Hepatology*, doi:10.1097/HEP.0000000000000520 (2023).

859 2 Devarbhavi, H. *et al.* Global burden of liver disease: 2023 update. *J Hepatol* **79**, 516-537,
860 doi:10.1016/j.jhep.2023.03.017 (2023).

861 3 Brahma, M. K. *et al.* Oxidative stress in obesity-associated hepatocellular carcinoma:
862 sources, signaling and therapeutic challenges. *Oncogene* **40**, 5155-5167, doi:10.1038/s41388-
863 021-01950-y (2021).

864 4 Talamantes, S. *et al.* Non-alcoholic fatty liver disease and diabetes mellitus as growing
865 aetiologies of hepatocellular carcinoma. *JHEP Rep* **5**, 100811,
866 doi:10.1016/j.jhepr.2023.100811 (2023).

867 5 Huang, D. Q. *et al.* Hepatocellular carcinoma surveillance - utilization, barriers and the
868 impact of changing aetiology. *Nat Rev Gastroenterol Hepatol*, doi:10.1038/s41575-023-
869 00818-8 (2023).

870 6 Gurzov, E. N., Stanley, W. J., Brodnicki, T. C. & Thomas, H. E. Protein tyrosine
871 phosphatases: molecular switches in metabolism and diabetes. *Trends Endocrinol Metab* **26**,
872 30-39, doi:10.1016/j.tem.2014.10.004 (2015).

873 7 Tonks, N. K. Protein tyrosine phosphatases--from housekeeping enzymes to master
874 regulators of signal transduction. *FEBS J* **280**, 346-378, doi:10.1111/febs.12077 (2013).

875 8 Li, S. *et al.* Cytoplasmic tyrosine phosphatase Shp2 coordinates hepatic regulation of bile
876 acid and FGF15/19 signaling to repress bile acid synthesis. *Cell Metab* **20**, 320-332,
877 doi:10.1016/j.cmet.2014.05.020 (2014).

878 9 Grohmann, M. *et al.* Obesity Drives STAT-1-Dependent NASH and STAT-3-Dependent
879 HCC. *Cell* **175**, 1289-1306 e1220, doi:10.1016/j.cell.2018.09.053 (2018).

880 10 Gurzov, E. N. *et al.* Hepatic oxidative stress promotes insulin-STAT-5 signaling and
881 obesity by inactivating protein tyrosine phosphatase N2. *Cell Metab* **20**, 85-102,
882 doi:10.1016/j.cmet.2014.05.011 (2014).

883 11 Young, K. A., Biggins, L. & Sharpe, H. J. Protein tyrosine phosphatases in cell adhesion.
884 *Biochem J* **478**, 1061-1083, doi:10.1042/BCJ20200511 (2021).

885 12 Brenachot, X. *et al.* Hepatic protein tyrosine phosphatase receptor gamma links obesity-
886 induced inflammation to insulin resistance. *Nat Commun* **8**, 1820, doi:10.1038/s41467-017-
887 02074-2 (2017).

888 13 Fearnley, G. W. *et al.* The homophilic receptor PTPRK selectively dephosphorylates
889 multiple junctional regulators to promote cell-cell adhesion. *Elife* **8**, doi:10.7554/eLife.44597
890 (2019).

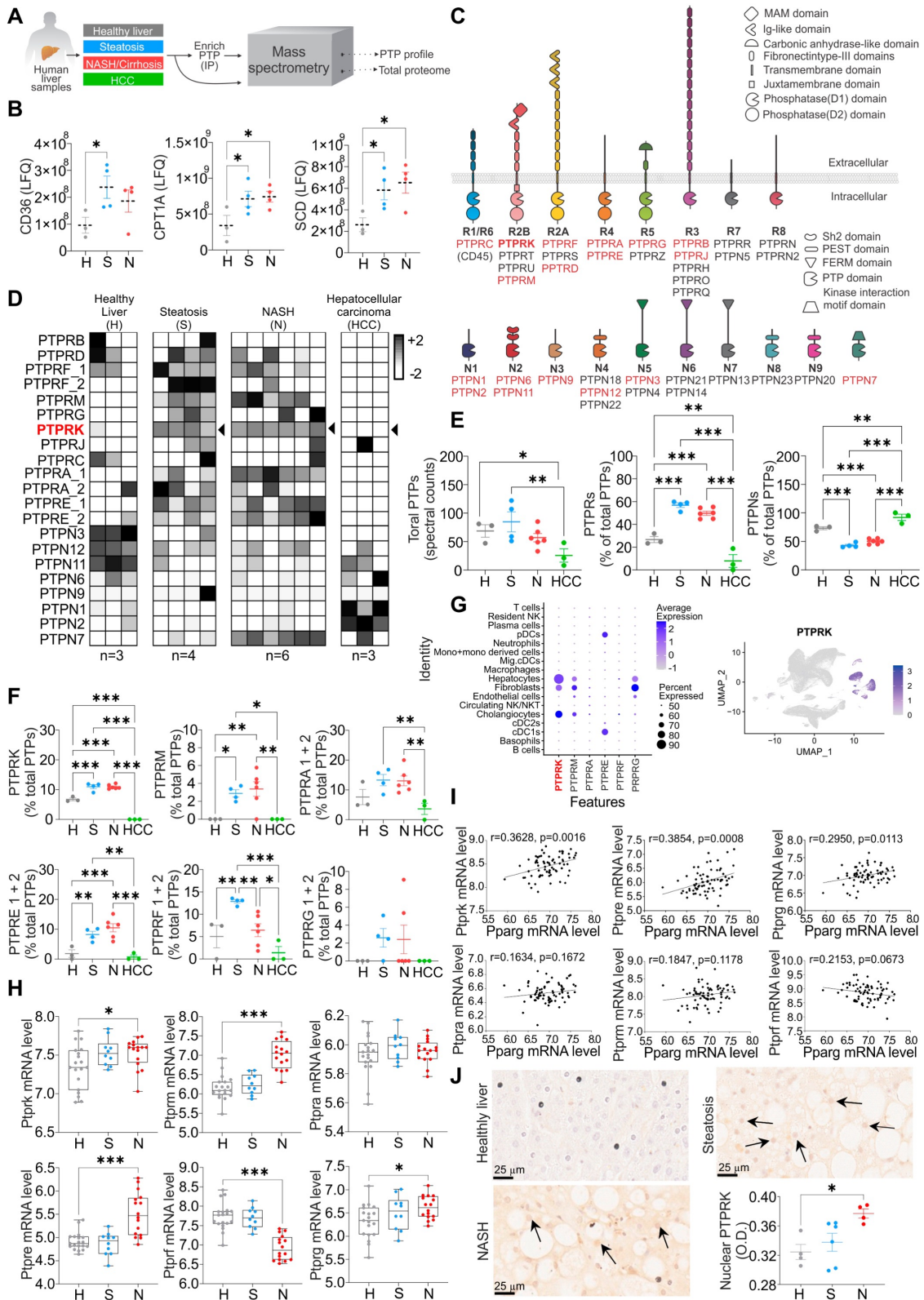
891 14 Trynka, G. *et al.* Dense genotyping identifies and localizes multiple common and rare
892 variant association signals in celiac disease. *Nat Genet* **43**, 1193-1201, doi:10.1038/ng.998
893 (2011).

894 15 Inshaw, J. R. J., Walker, N. M., Wallace, C., Bottolo, L. & Todd, J. A. The chromosome
895 6q22.33 region is associated with age at diagnosis of type 1 diabetes and disease risk in those

- 896 diagnosed under 5 years of age. *Diabetologia* **61**, 147-157, doi:10.1007/s00125-017-4440-y
897 (2018).
- 898 16 Anders, L. *et al.* Furin-, ADAM 10-, and gamma-secretase-mediated cleavage of a receptor
899 tyrosine phosphatase and regulation of beta-catenin's transcriptional activity. *Mol Cell Biol*
900 **26**, 3917-3934, doi:10.1128/MCB.26.10.3917-3934.2006 (2006).
- 901 17 Xu, Y., Xue, S., Zhou, J., Voorhees, J. J. & Fisher, G. J. Notch and TGF-beta pathways
902 cooperatively regulate receptor protein tyrosine phosphatase-kappa (PTPRK) gene expression
903 in human primary keratinocytes. *Mol Biol Cell* **26**, 1199-1206, doi:10.1091/mbc.E14-12-1591
904 (2015).
- 905 18 Guilliams, M. *et al.* Spatial proteogenomics reveals distinct and evolutionarily conserved
906 hepatic macrophage niches. *Cell* **185**, 379-396 e338, doi:10.1016/j.cell.2021.12.018 (2022).
- 907 19 Barclay, J. L. *et al.* GH-dependent STAT5 signaling plays an important role in hepatic lipid
908 metabolism. *Endocrinology* **152**, 181-192, doi:10.1210/en.2010-0537 (2011).
- 909 20 Hasenfuss, S. C. *et al.* Regulation of steatohepatitis and PPARgamma signaling by distinct
910 AP-1 dimers. *Cell Metab* **19**, 84-95, doi:10.1016/j.cmet.2013.11.018 (2014).
- 911 21 Li, F. *et al.* FBP1 loss disrupts liver metabolism and promotes tumorigenesis through a
912 hepatic stellate cell senescence secretome. *Nat Cell Biol* **22**, 728-739, doi:10.1038/s41556-
913 020-0511-2 (2020).
- 914 22 Koberstein, J. N. *et al.* Monitoring glycolytic dynamics in single cells using a fluorescent
915 biosensor for fructose 1,6-bisphosphate. *Proc Natl Acad Sci U S A* **119**, e2204407119,
916 doi:10.1073/pnas.2204407119 (2022).
- 917 23 Valenti, L. *et al.* Hepatic notch signaling correlates with insulin resistance and nonalcoholic
918 fatty liver disease. *Diabetes* **62**, 4052-4062, doi:10.2337/db13-0769 (2013).
- 919 24 Regnier, M., Carbinatti, T., Parlati, L., Benhamed, F. & Postic, C. The role of ChREBP in
920 carbohydrate sensing and NAFLD development. *Nat Rev Endocrinol* **19**, 336-349,
921 doi:10.1038/s41574-023-00809-4 (2023).
- 922 25 Yang, F. *et al.* Metabolic reprogramming and its clinical implication for liver cancer.
923 *Hepatology*, doi:10.1097/HEP.0000000000000005 (2023).
- 924 26 Guertin, D. A. & Wellen, K. E. Acetyl-CoA metabolism in cancer. *Nat Rev Cancer* **23**,
925 156-172, doi:10.1038/s41568-022-00543-5 (2023).
- 926 27 Luo, X. *et al.* The fatty acid receptor CD36 promotes HCC progression through activating
927 Src/PI3K/AKT axis-dependent aerobic glycolysis. *Cell Death Dis* **12**, 328,
928 doi:10.1038/s41419-021-03596-w (2021).
- 929 28 Broadfield, L. A. *et al.* Fat Induces Glucose Metabolism in Nontransformed Liver Cells
930 and Promotes Liver Tumorigenesis. *Cancer Res* **81**, 1988-2001, doi:10.1158/0008-
931 5472.CAN-20-1954 (2021).
- 932 29 Martinez-Reyes, I. & Chandel, N. S. Mitochondrial TCA cycle metabolites control
933 physiology and disease. *Nat Commun* **11**, 102, doi:10.1038/s41467-019-13668-3 (2020).
- 934 30 Stine, Z. E., Schug, Z. T., Salvino, J. M. & Dang, C. V. Targeting cancer metabolism in
935 the era of precision oncology. *Nat Rev Drug Discov* **21**, 141-162, doi:10.1038/s41573-021-
936 00339-6 (2022).
- 937 31 Chen, Y. W. *et al.* Receptor-type tyrosine-protein phosphatase kappa directly targets
938 STAT3 activation for tumor suppression in nasal NK/T-cell lymphoma. *Blood* **125**, 1589-
939 1600, doi:10.1182/blood-2014-07-588970 (2015).
- 940 32 Yuan, Y. *et al.* alpha-Ketoglutaric acid ameliorates hyperglycemia in diabetes by inhibiting
941 hepatic gluconeogenesis via serpinale signaling. *Sci Adv* **8**, eabn2879,
942 doi:10.1126/sciadv.abn2879 (2022).
- 943 33 Morris, J. P. t. *et al.* alpha-Ketoglutarate links p53 to cell fate during tumour suppression.
944 *Nature* **573**, 595-599, doi:10.1038/s41586-019-1577-5 (2019).

- 945 34 Brownstein, A. J., Veliova, M., Acin-Perez, R., Liesa, M. & Shirihai, O. S. ATP-consuming
946 futile cycles as energy dissipating mechanisms to counteract obesity. *Rev Endocr Metab*
947 *Disord* **23**, 121-131, doi:10.1007/s11154-021-09690-w (2022).
- 948 35 Stanford, S. M. & Bottini, N. Targeting protein phosphatases in cancer immunotherapy and
949 autoimmune disorders. *Nat Rev Drug Discov* **22**, 273-294, doi:10.1038/s41573-022-00618-w
950 (2023).
- 951 36 Liang, S. *et al.* A small molecule inhibitor of PTP1B and PTPN2 enhances T cell anti-
952 tumor immunity. *Nat Commun* **14**, 4524, doi:10.1038/s41467-023-40170-8 (2023).
- 953 37 Baumgartner, C. K. *et al.* The PTPN2/PTPN1 inhibitor ABBV-CLS-484 unleashes potent
954 anti-tumour immunity. *Nature*, doi:10.1038/s41586-023-06575-7 (2023).
- 955 38 Qian, Z. *et al.* Manipulating PTPRD function with ectodomain antibodies. *Genes Dev* **37**,
956 743-759, doi:10.1101/gad.350713.123 (2023).
- 957 39 Powell, E. E., Wong, V. W. & Rinella, M. Non-alcoholic fatty liver disease. *Lancet* **397**,
958 2212-2224, doi:10.1016/S0140-6736(20)32511-3 (2021).
- 959 40 Fendt, S. M. *et al.* Reductive glutamine metabolism is a function of the alpha-ketoglutarate
960 to citrate ratio in cells. *Nat Commun* **4**, 2236, doi:10.1038/ncomms3236 (2013).
- 961 41 Quaegebeur, A. *et al.* Deletion or Inhibition of the Oxygen Sensor PHD1 Protects against
962 Ischemic Stroke via Reprogramming of Neuronal Metabolism. *Cell Metab* **23**, 280-291,
963 doi:10.1016/j.cmet.2015.12.007 (2016).
- 964 42 Jung, Y., Zhao, M. & Svensson, K. J. Isolation, culture, and functional analysis of
965 hepatocytes from mice with fatty liver disease. *STAR Protoc* **1**, 100222,
966 doi:10.1016/j.xpro.2020.100222 (2020).
- 967 43 Post, H. *et al.* Robust, Sensitive, and Automated Phosphopeptide Enrichment Optimized
968 for Low Sample Amounts Applied to Primary Hippocampal Neurons. *J Proteome Res* **16**,
969 728-737, doi:10.1021/acs.jproteome.6b00753 (2017).
- 970 44 Karpievitch, Y. V. *et al.* Normalization of peak intensities in bottom-up MS-based
971 proteomics using singular value decomposition. *Bioinformatics* **25**, 2573-2580,
972 doi:10.1093/bioinformatics/btp426 (2009).
- 973 45 Hao, Y. *et al.* Dictionary learning for integrative, multimodal and scalable single-cell
974 analysis. *Nat Biotechnol*, doi:10.1038/s41587-023-01767-y (2023).
- 975 46 Kechin, A., Boyarskikh, U., Kel, A. & Filipenko, M. cutPrimers: A New Tool for Accurate
976 Cutting of Primers from Reads of Targeted Next Generation Sequencing. *J Comput Biol* **24**,
977 1138-1143, doi:10.1089/cmb.2017.0096 (2017).
- 978 47 Dobin, A. *et al.* STAR: ultrafast universal RNA-seq aligner. *Bioinformatics* **29**, 15-21,
979 doi:10.1093/bioinformatics/bts635 (2013).
- 980 48 Robinson, M. D., McCarthy, D. J. & Smyth, G. K. edgeR: a Bioconductor package for
981 differential expression analysis of digital gene expression data. *Bioinformatics* **26**, 139-140,
982 doi:10.1093/bioinformatics/btp616 (2010).
- 983 49 Hay, I. M. *et al.* The receptor PTPRU is a redox sensitive pseudophosphatase. *Nat Commun*
984 **11**, 3219, doi:10.1038/s41467-020-17076-w (2020).
- 985 50 Wang, Y. *et al.* Defined and Scalable Generation of Hepatocyte-like Cells from Human
986 Pluripotent Stem Cells. *J Vis Exp*, doi:10.3791/55355 (2017).
- 987
988
989

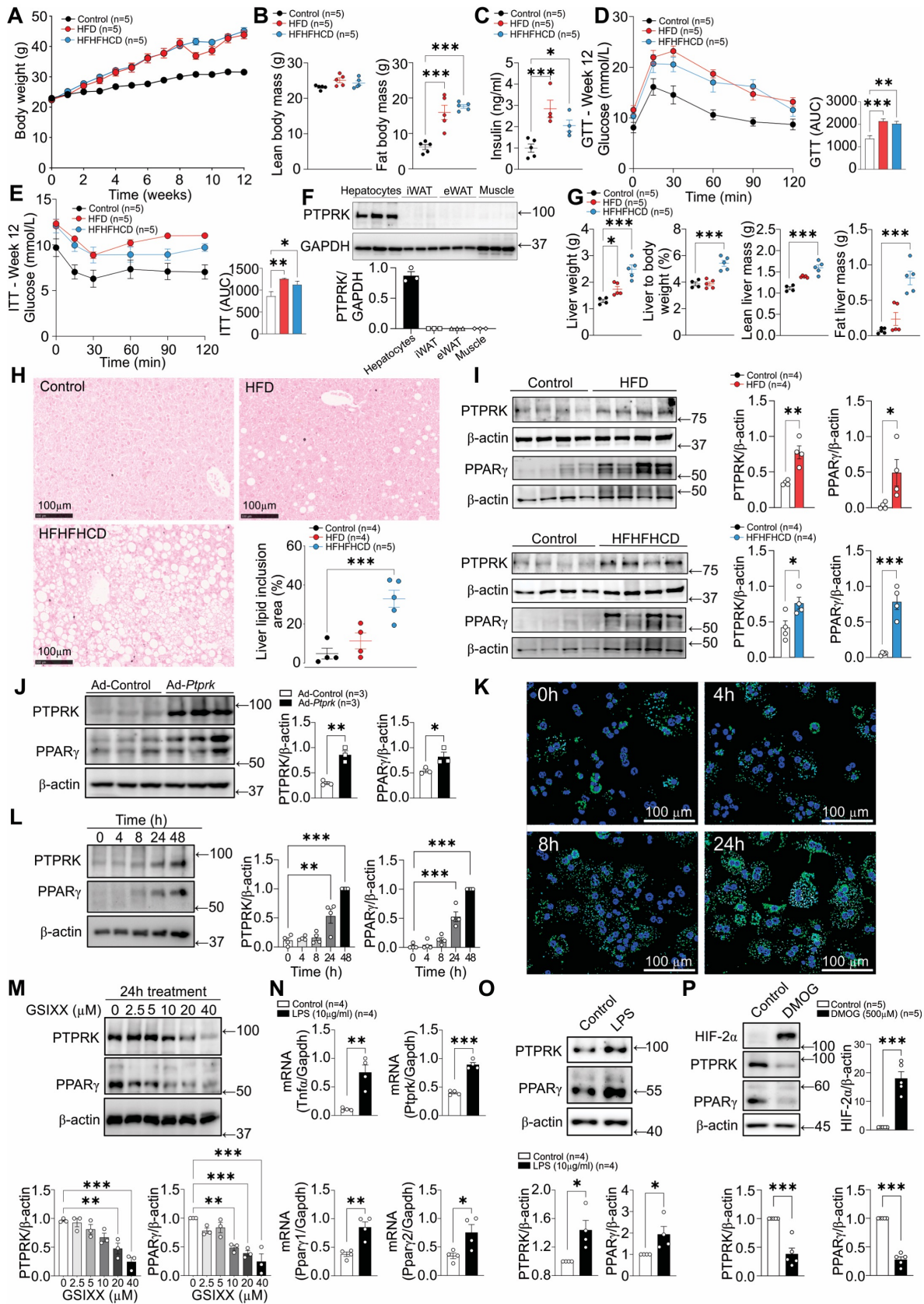
990 Figures:



991

992 **Figure 1 – Enhanced PTPRK expression in human livers with steatosis and non-alcoholic**
 993 **steatohepatitis (NASH).** (A) Methodological approach schematic illustrating the

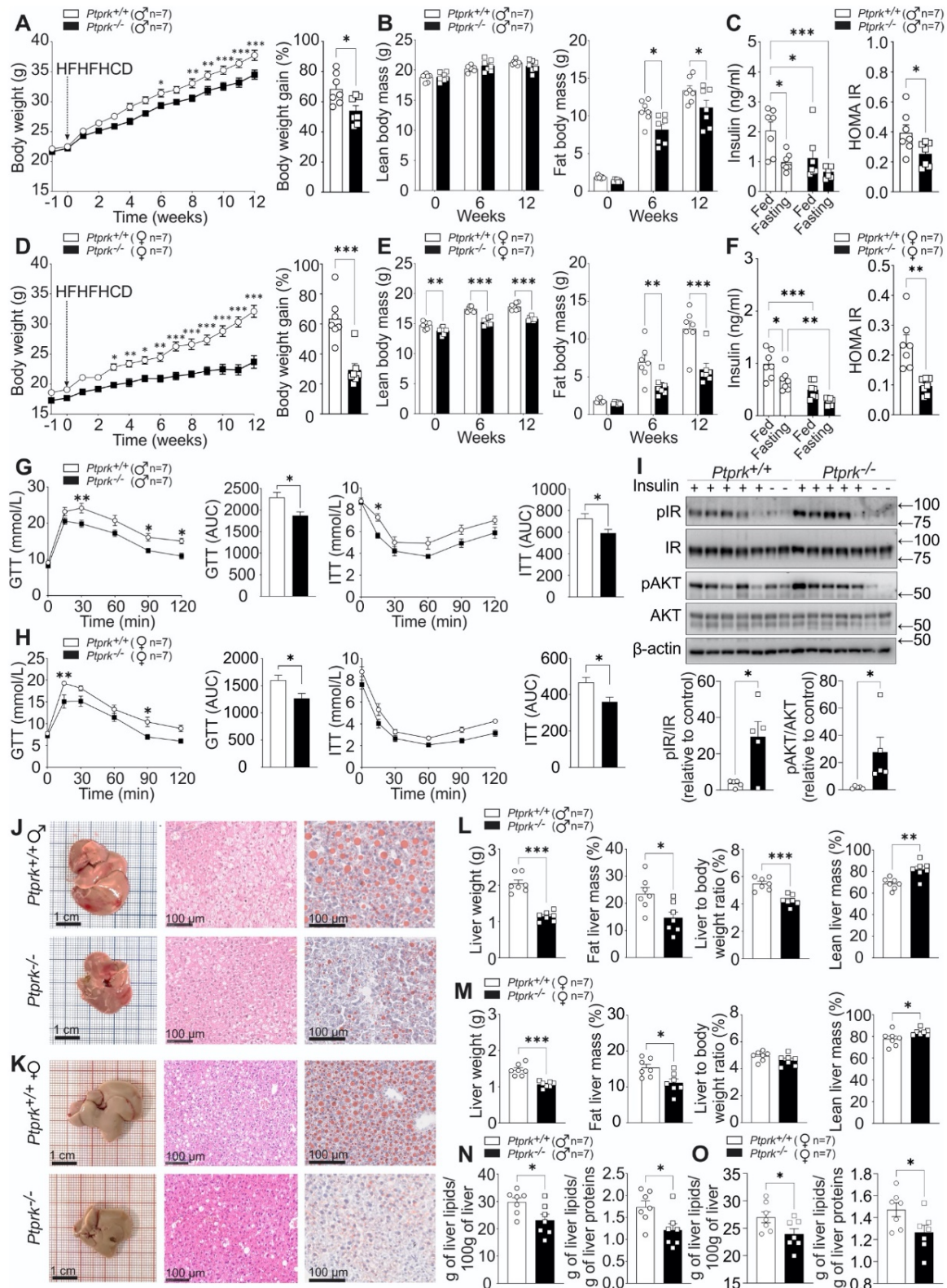
994 quantification of protein tyrosine phosphatase (PTP) profile and total proteome in human
995 livers. **(B)** Quantification of lipid metabolism-related proteins using label-free quantification
996 (LFQ) in healthy (H), steatotic (S) and NASH (N) livers. **(C)** Schematic representation of PTP
997 families and their characteristic domains. PTPs detected by mass spectrometry are labelled in
998 red. **(D)** Heat map displaying the hepatic PTP profile. **(E)** Spectral counts of total PTPs and
999 the proportional contribution of receptor and non-receptor PTPs among the identified PTPs.
1000 **(F)** The proportional contribution of PTPRK and other receptor PTPs to the total identified
1001 PTPs is shown. **(G)** Data extracted from GSE192740 showing hepatocyte expression of
1002 PTPRK. **(H)** RPTP mRNA levels in the E-MEXP-3291 dataset. **(I)** Correlation analysis
1003 between RPTPs and Pparg mRNA levels in the E-GEOD-48452 dataset. **(J)** Representative
1004 immunohistochemistry (IHC) images displaying PTPRK staining and quantitative results for
1005 nuclear PTPRK. Statistical significance is denoted as $*p<0.05$, $**p<0.01$, $***p<0.001$.
1006



1007

1008 **Figure 2 - Hepatocyte PTPRK is induced by Notch signalling and LPS, correlating**
 1009 **positively with PPAR γ in obese mouse models and primary hepatocytes. (A-E).** 8-week
 1010 old C57BL6N mice were fed either a high-fat diet (HFD) or a high-fat high-fructose high-
 1011 cholesterol diet (HFHFHCD) for 12 weeks. We measured (A) body weight, (B) body
 1012 composition, and (C) fasting insulinemia. Mice underwent (D) glucose and (E) insulin

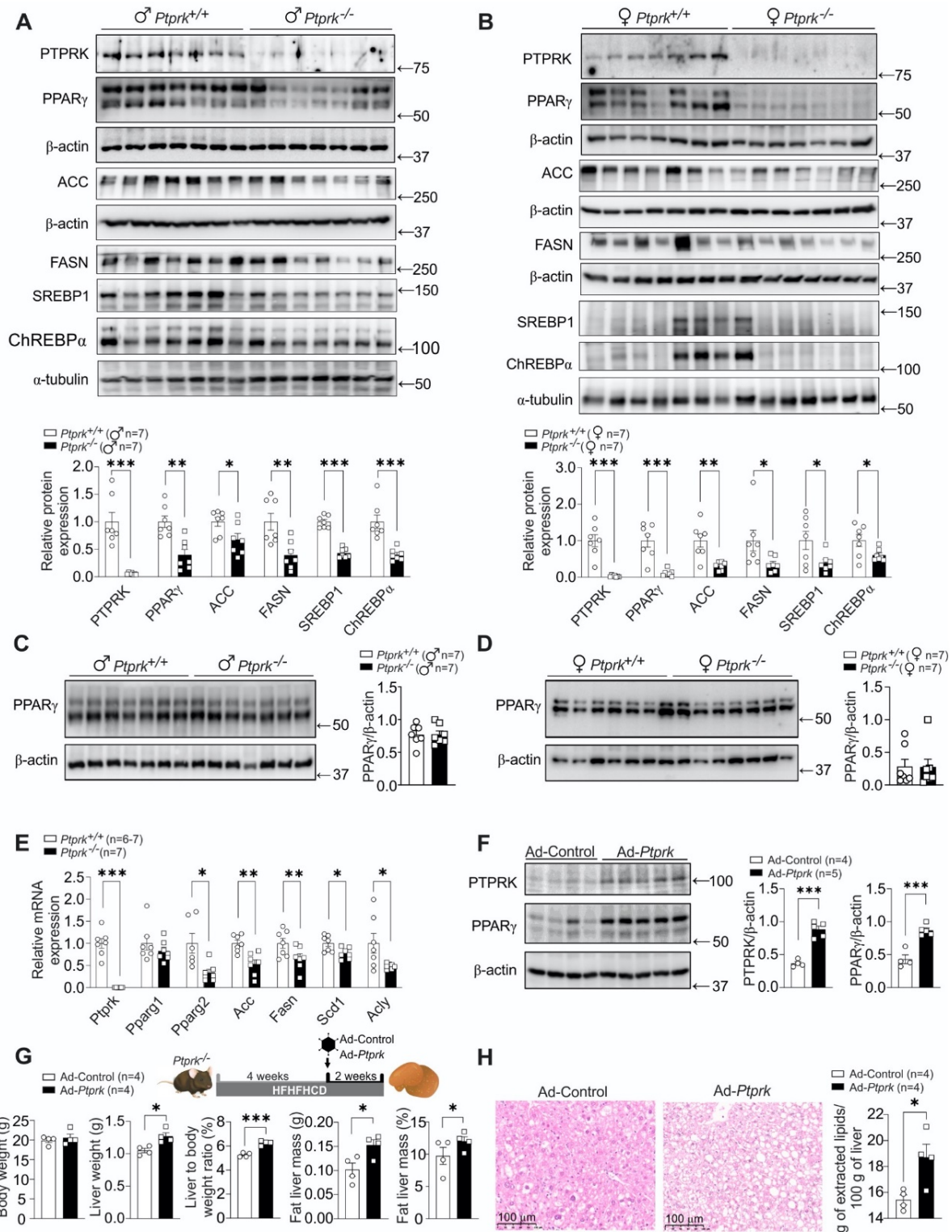
1013 tolerance tests after 12 weeks of diet. **(F)** Primary hepatocytes, inguinal white adipose tissue
1014 (iWAT), epididymal white adipose tissue (eWAT), and gastrocnemius (muscle) were
1015 harvested for immunoblot analysis of PTPRK. **(G)** The livers were extracted and assessed for
1016 liver weight and composition. **(H)** Histological analysis was conducted to quantify the
1017 vacuolation area, serving as an indicator of hepatic lipid inclusions. **(I)** Immunoblot analysis
1018 was carried out to determine the levels of PTPRK and PPAR γ . **(J)** 8-week-old C57BL6N mice
1019 receiving a chow (control) diet were transduced with an adenoviral vector to induce PTPRK
1020 overexpression (*Ad-Ptprk*). Two weeks later, immunoblot analysis was performed in liver
1021 samples to assess the levels of PTPRK and PPAR γ . **(K)** Primary mouse hepatocytes were
1022 cultured overnight under standard conditions and fixed at different time points (0, 4, 8, and
1023 24h) for Nile Red staining to visualise lipid droplets. **(L)** Immunoblot analysis of PTPRK and
1024 PPAR γ was performed on primary mouse hepatocytes collected at different time points as
1025 indicated. **(M)** Primary mouse hepatocytes were cultured overnight and treated with different
1026 concentrations of the Notch signalling inhibitor GSIXX for 24h. Immunoblot analysis was
1027 employed to evaluate the expression levels of PTPRK and PPAR γ . **(N, O)** Primary mouse
1028 hepatocytes were cultured overnight and treated with lipopolysaccharide (LPS) for 24h. The
1029 gene expression was analysed by quantitative PCR (qPCR, **N**) or immunoblot techniques (**O**).
1030 **(P)** Primary mouse hepatocytes were cultured overnight and treated with
1031 dimethylxalylglycine (DMOG), an inhibitor of 2-oxoglutarate-dependent dioxygenases
1032 required for hypoxia-inducible factor (HIF) degradation, for 24h. Immunoblot analysis was
1033 performed to examine the expression of HIF2 α , PTPRK, and PPAR γ . Statistical significance
1034 is denoted as * p <0.05, ** p <0.01, *** p <0.001.



1035

1036 **Figure 3 – PTPRK deletion confers protection against diet-induced obesity, insulin**
 1037 **resistance, and hepatic steatosis. (A-H)** Male (♂) and female (♀) C57BL6N $Ptprk^{+/+}$ and
 1038 $Ptprk^{-/-}$ mice, aged 8 weeks, were subjected to a high-fat, high-fructose, high-cholesterol diet
 1039 (HFHFHCD) for a period of 12 weeks. We measured body weight (**A, D**), body composition
 1040 (**B, E**), insulinemia (**C, F**), and performed glucose and insulin tolerance tests (**G, H**). (**I**) At
 1041 the end of HFHFHCD feeding, insulin was administered to female mice 10 min prior to liver
 1042 collection. Immunoblot analysis was employed to examine the expression of pIR and pAKT

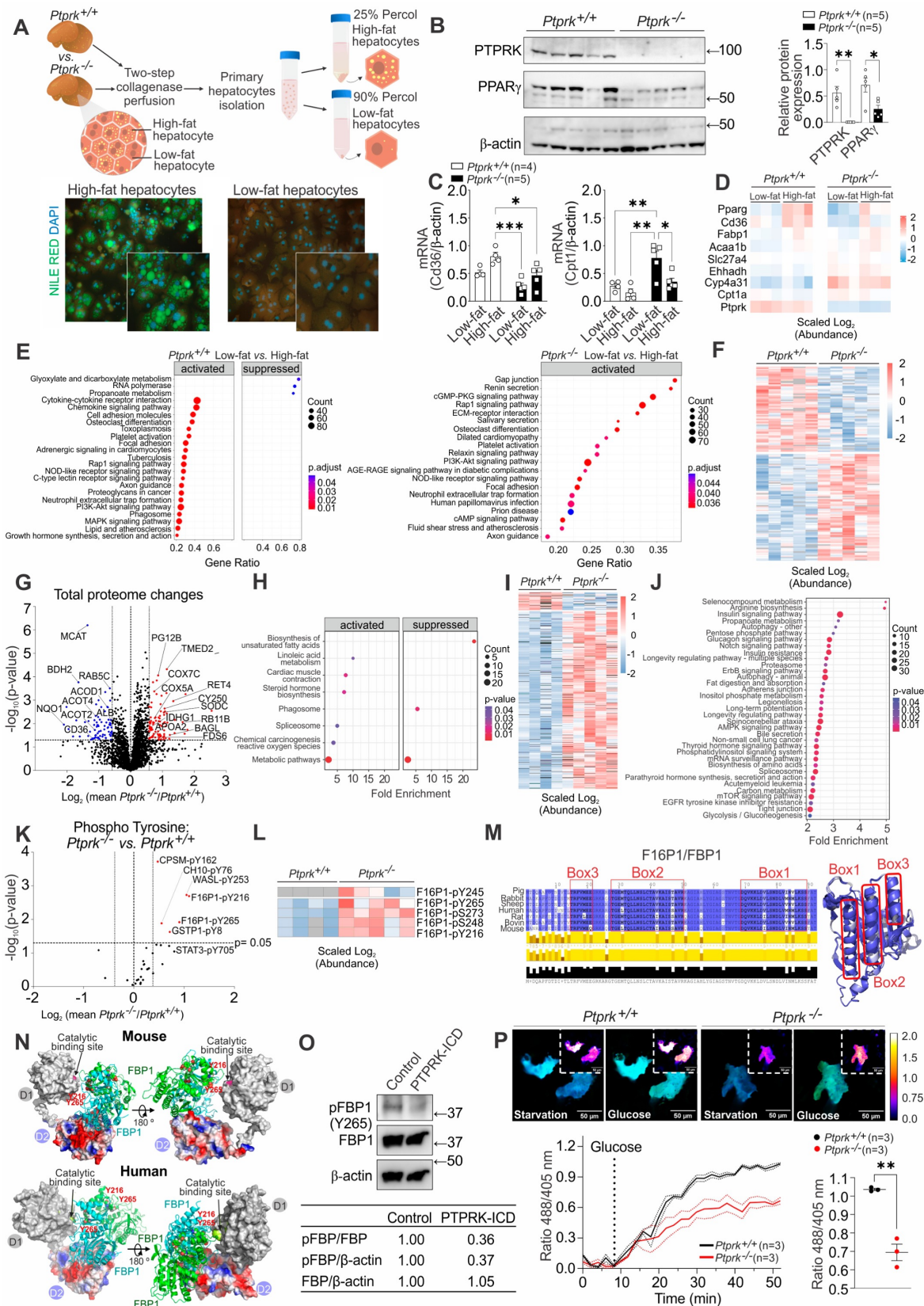
1043 in the liver. (**J-O**) Liver samples were analysed to assess fat accumulation through histological
1044 examination (**J, K**), measurements of liver weight and composition (**L, M**), and total liver
1045 lipid extraction (**N, O**). (**I**). Statistical significance is denoted as * $p < 0.05$, ** $p < 0.01$,
1046 *** $p < 0.001$.



1047

1048 **Figure 4 – PTPRK orchestrates the hepatic expression of metabolic enzymes and**
 1049 **transcription factors promoting steatosis in mice fed an obesogenic diet. (A, B)** Eight-
 1050 week-old male (♂) and female (♀) C57BL6N $Ptpdk^{+/+}$ and $Ptpdk^{-/-}$ were exposed to a high-
 1051 fat, high-fructose, high-cholesterol diet (HFHFHCD) for 12 weeks. Liver samples were
 1052 analysed to examine the levels of PTPRK, PPAR γ , ACC (Acetyl-CoA Carboxylase), FASN
 1053 (Fatty Acid Synthase), SREBP1 (Sterol Regulatory Element-Binding Protein 1), and ChREBP
 1054 (Carbohydrate Response Element-Binding Protein). (C, D) Subcutaneous (inguinal fat, C and
 1055 D) white adipose tissues were collected for immunoblot analysis of PPAR γ . (E) Liver mRNA
 1056 expression of *Ptpdk*, *Pparg*, *Acc*, *Fasn*, *Scd1* (Stearoyl-CoA Desaturase 1), and *Acl1* (ATP

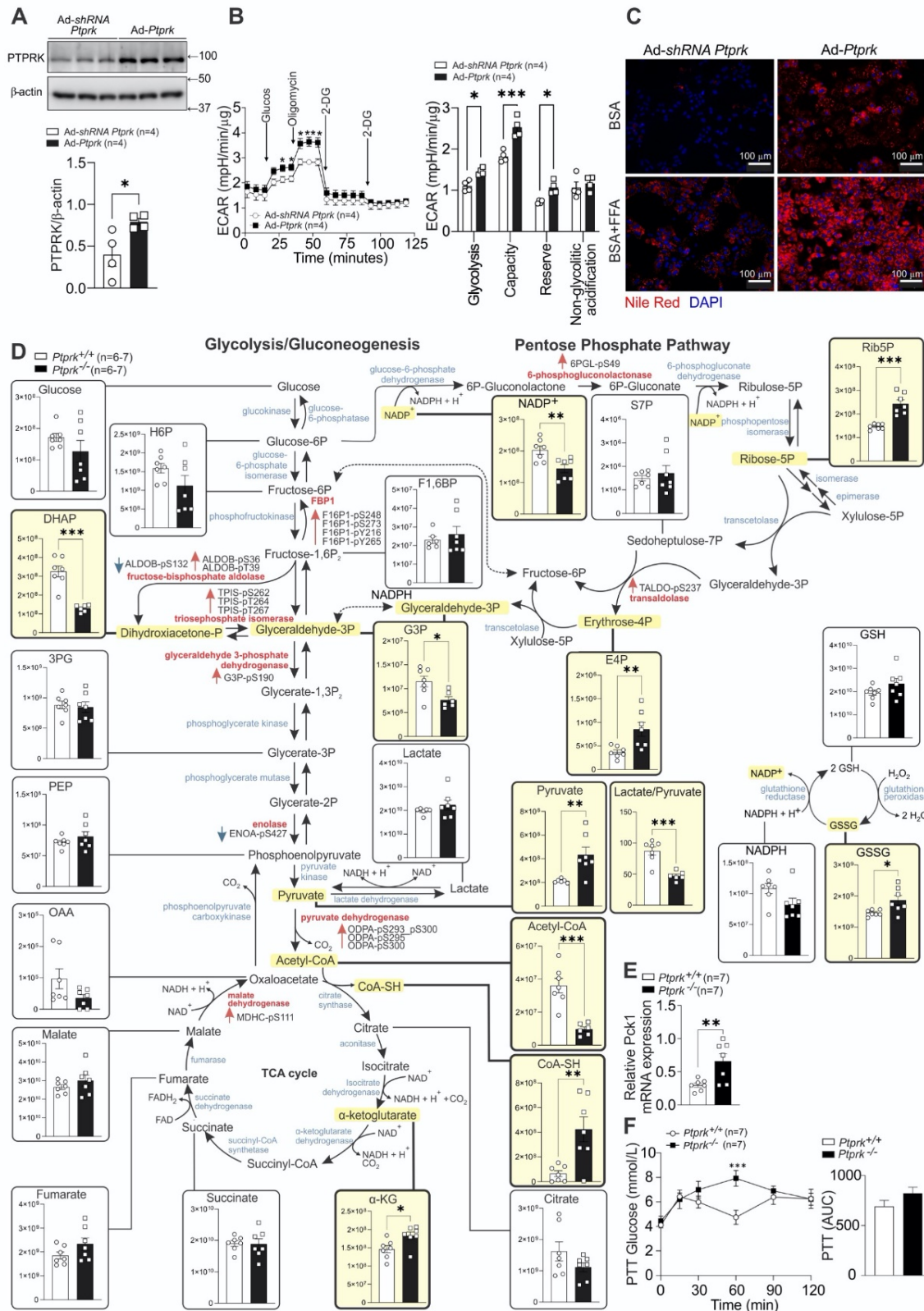
1057 Citrate Lyase) was assessed. (F) Mice were subjected to HFHFHCD for four weeks and were
1058 administered an adenoviral vector to induce PTPRK overexpression (*Ad-Ptprk*). After a 2-
1059 week period, liver samples were collected for immunoblot analysis of PTPRK and PPAR γ .
1060 (G) PTPRK knockout mice were subjected to HFHFHCD for four weeks and subsequently
1061 injected with *Ad-Ptprk*. After an additional two weeks on HFHFHCD, body weight was
1062 measured, and liver were collected for the evaluation of weight and composition. (H) Liver
1063 histological assessment and total lipid extraction were performed after PTPRK
1064 overexpression. Statistical significance is indicated as * $p < 0.05$, ** $p < 0.01$, *** $p < 0.001$.
1065



1066

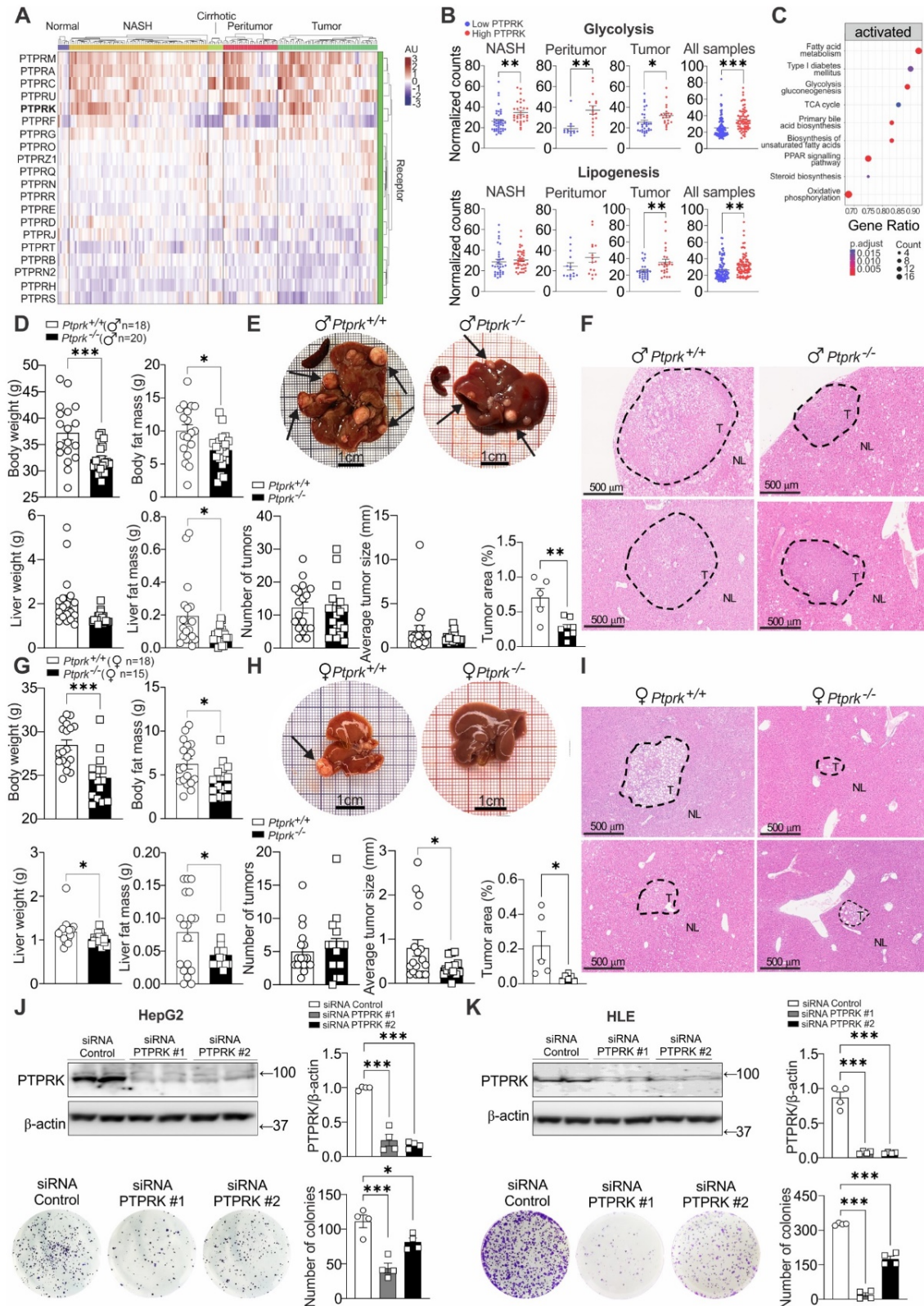
1067 **Figure 5 – Comprehensive analysis of the transcriptome, proteome, and protein**
 1068 **phosphorylation changes in primary hepatocytes isolated from livers of *Ptprk*^{-/-} and**
 1069 ***Ptprk*^{+/+} mice. (A) Methodological approach schematic illustrating the isolation of primary**
 1070 **hepatocytes from mice fed HFHFHCD for 12 weeks, followed by separation based on cell**

1071 density into hepatocytes with high-fat content and hepatocytes with low-fat content. **(B)**
1072 Immunoblot analysis revealing PTPRK and PPAR γ expression profiles of hepatocytes with
1073 high-fat content. **(C)** RT-qPCR analysis depicting changes in the expression of lipid
1074 metabolism-related genes. **(D)** RNA-Seq heatmap displaying alterations in PPAR pathway-
1075 related genes. **(E)** RNA-Seq KEGG pathway enrichment analysis comparing *Ptprk*^{+/+} low-fat
1076 vs. high-fat hepatocytes (left side) and the same comparison in *Ptprk*^{-/-} hepatocytes (right side).
1077 **(F)** Total proteome global heatmap showing significantly altered proteins. **(G)** Volcano plot
1078 illustrating the changes in the total proteomic profile between *Ptprk*^{-/-} and *Ptprk*^{+/+} high-fat
1079 hepatocytes. **(H)** Total proteome KEGG pathway enrichment analysis. **(I)** Phosphoproteome
1080 global heatmap showing significantly altered phosphoproteins. **(J)** Phosphoproteome KEGG
1081 pathway enrichment analysis. **(K)** Volcano plot displaying only the quantification of tyrosine
1082 phosphosites in *Ptprk*^{-/-} and *Ptprk*^{+/+} hepatocytes. Phosphosites with over 30% increase in
1083 *Ptprk*^{-/-} cells are marked in red ($p < 0.05$). **(L)** Heatmap showcasing the significantly changing
1084 phosphopeptides in fructose-1,6-bisphosphatase 1 (F16P1/FBP1). **(M)** Schematic
1085 representation of different F16P1/FBP1 amino acid sequences, indicating distinct boxes for
1086 interaction mapping experiments. The predicted helical regions are depicted in the three-
1087 dimensional structure on the right side. **(N)** Conservation mapping of the predicted PTPRK-
1088 FBP1 interface, illustrating the PTPRK-D2 complex (red, blue, and grey surface
1089 representation of their electrostatic surface potential) interacting with the FBP1 dimer (light
1090 green and light blue) and the proximity of the PTPRK catalytic site and increased FBP1
1091 phosphotyrosine residues. The D1 domain of PTPRK is shown in grey surface representation.
1092 **(O)** Immunoblot analysis of pervanadate-treated mouse hepatocyte lysates incubated with or
1093 without the recombinant PTPRK-ICD (ICD: intracellular domain) prior to pFBP1 (Y265)
1094 analysis **(P)** Primary mouse hepatocytes were transfected with HYlight to monitor fructose
1095 1,6-bisphosphate dynamics. After injection of 20 mM glucose, fluorescence ratios (R_{488}/R_{405})
1096 were calculated and Min-Max normalized. Solid lines represent the mean across cells, while
1097 dots represent the mean \pm SEM. The presented data represent the average of multiple
1098 independent biological replicates. Statistical significance in panels **B**, **C**, and **P** is indicated
1099 as * $p < 0.05$, ** $p < 0.01$, *** $p < 0.001$.
1100



1101
 1102 **Figure 6 - Hepatic PTPRK induces metabolic reprogramming in the livers of mice fed**
 1103 **an obesogenic diet.** (A) Primary mouse hepatocytes were cultured and transduced with an
 1104 adenoviral vector to induce either PTPRK overexpression (*Ad-Ptprk*) or silencing of PTPRK
 1105 (*Ad-shRNA Ptprk*). Immunoblotting (triplicates representative of 4 independent experiments)
 1106 confirmed the modulation of PTPRK expression and (B) real-time measurement of

1107 extracellular acidification rate (ECAR) in response to glycolytic modulators, revealed changes
1108 in glycolytic parameters. (C) Primary mouse hepatocytes were treated with a mixture of BSA-
1109 conjugated fatty acids, palmitate (PA), and oleate (OA) (0.4 mM PA and 0.8 mM OA) to
1110 simulate triglyceride deposition, and subsequently stained with Nile Red to visualize lipid
1111 droplets rich in neutral lipids (triglycerides). (D) Untargeted metabolomics analysis was
1112 conducted in mouse livers from *Ptprk*^{-/-} and *Ptprk*^{+/+} female mice fed HFHFHCD for 12
1113 weeks. Metabolites exhibiting statistically significant changes are highlighted (light yellow).
1114 The data is presented as raw abundances corrected for sample weight. Enzymes associated
1115 with these metabolites, which showed significant differences in the levels of phosphorylated
1116 amino acids based on the analysis presented in Figure 5I, are indicated in red. Red arrows near
1117 highlighted enzymes indicate increased phosphorylation at specific amino acid residues, while
1118 blue arrows indicate reduced phosphorylation at those respective residues. (E) qPCR analysis
1119 was performed to assess *Pck1* mRNA levels in the livers of *Ptprk*^{-/-} and *Ptprk*^{+/+} mice. (F) A
1120 pyruvate tolerance test was conducted in mice fed HFHFHCD for 12 weeks after overnight
1121 fasting to assess their gluconeogenic capacity in response to pyruvate administration.
1122 Statistical significance is indicated as **p*<0.05, ***p*<0.01, ****p*<0.001.
1123



1124

1125 **Figure 7 – Influence of PTPRK in hepatocellular carcinoma (HCC) development.** (A)
 1126 RPTP mRNA expression profiling was conducted on human livers from dataset GSE164760
 1127 encompassing various stages of obesity-associated liver dysfunction and
 1128 hepatocarcinogenesis, including normal liver, non-alcoholic steatohepatitis (NASH), cirrhotic
 1129 livers, peritumour regions, and hepatocellular carcinoma (HCC) tumours. (B) Based on the

1130 expression levels of PTPRK, the samples were categorized as high or low, and the normalized
1131 counts of genes involved in glycolysis/gluconeogenesis and lipogenesis were analysed. (C)
1132 KEGG pathway enrichment analysis was performed specifically on tumour samples with low
1133 or high PTPRK expression levels. (D-I) Male and female *Ptprk*^{-/-} and *Ptprk*^{+/+} mice were
1134 subjected to diethylnitrosamine (DEN) induction of liver cancer at 2 weeks of age. Tumour
1135 development was assessed when the animals reached 40 weeks of age. Measurements of body
1136 weight, fat body mass, liver weight, and fat liver mass were recorded (D, G). Tumours on the
1137 hepatic lobes were quantified and measured, considering tumours bigger than 0.2mm. The
1138 results are presented as the number of tumours per liver and the average tumour size (E, H).
1139 Microscopic tumours were quantified through histological analysis. Representative H&E-
1140 stained sections showing nodules (F, I). (J, K) Human hepatoma cell lines HepG2 (J) and
1141 HLE (K) were transfected with siRNAs targeting PTPRK or siRNA control, and colony-
1142 forming capacity was assessed. Immunoblot analysis confirmed the efficiency of transfection,
1143 and crystal violet staining was employed to visualise and quantify the colonies. Statistical
1144 significance is indicated as * $p < 0.05$, ** $p < 0.01$, *** $p < 0.001$.
1145